

DeepONet: Learning nonlinear operators based on the universal approximation theorem of operators

Lu Lu¹, Pengzhan Jin², Guofei Pang¹, Zhongqiang Zhang³, and George Em Karniadakis^{1,*}

¹Division of Applied Mathematics, Brown University, Providence, RI 02912, USA

²LSEC, ICMSEC, Academy of Mathematics and Systems Science, Chinese Academy of Sciences, Beijing 100190, China

³Department of Mathematical Sciences, Worcester Polytechnic Institute, Worcester, MA 01609, USA

*e-mail: george_karniadakis@brown.edu

Abstract

It is widely known that neural networks (NNs) are universal approximators of continuous functions, however, a less known but powerful result is that a NN with a single hidden layer can approximate accurately any nonlinear continuous operator. This universal approximation theorem of operators is suggestive of the potential of NNs in learning from scattered data any continuous operator or complex system. To realize this theorem, we design a new NN with small generalization error, the deep operator network (DeepONet), consisting of a NN for encoding the discrete input function space (branch net) and another NN for encoding the domain of the output functions (trunk net). We demonstrate that DeepONet can learn various explicit operators, e.g., integrals and fractional Laplacians, as well as implicit operators that represent deterministic and stochastic differential equations. We study, in particular, different formulations of the input function space and its effect on the generalization error.

Introduction

Over the last three centuries, mathematical models based on calculus have been employed to both predict and interpret physical phenomena around us, establishing fundamental laws that generalize well. Reflecting on the 25 centuries of mathematics, from the Pythagoreans, to Newton's law, and relativity theories or the uncertainty principle, new descriptions of physical phenomena have followed the mathematics prevalent at that time together with prior knowledge. While calculus has served science well, new fundamental developments are slow and have not established any governing principles in some fields, e.g., in the emerging field of social dynamics. In the era of artificial intelligence and data analytics, the question is then if there are any more expressive representations that can be employed to accelerate scientific discovery. Classical calculus and partial differential equations (PDEs) or their stochastic variants, taught diligently in colleges around the globe, have been effective in the era of the "pursuit of simplicity" [39], but they may be inefficient or even inadequate to represent complex inter-connected systems or systems of systems with non-local interactions [42]. There is nothing unique about the calculus we use currently, and a concrete example is offered in [12], where the same set of data can be represented with the same accuracy by either an integer-order three-term PDE (in the form of the familiar advection-diffusion system)

or by an unfamiliar two-term fractional order PDE, hence using the more expressive fractional calculus for discovering a new more compact PDE for time-dependent advection-diffusion systems.

Here, we investigate the possibility of formulating an alternative *calculus-agnostic* simple and fast way of describing an operator and its dynamics implicitly based on a give data set. More broadly, with the anticipated frequent human-robot interactions in the not too distant future, we address the question on how to best educate the new generations on quantitative inference and how to endow new robots with the required intelligence. Following the current paradigm, one approach would be to teach robots calculus, i.e., one integral or differential operator at a time, and train them to synthesize and solve such PDEs at blazing speeds to make quantitative decisions, sense their environment, and communicate with humans; however, this seems computationally prohibitive. An alternative direction is to train them using new means in learning nonlinear operators and functionals that compactly express very complex dynamics without the need for resorting to prior knowledge of 17th-century calculus. A similar paradigm for discovering new physics concepts with no prior knowledge was provided in [17] using NNs and representation learning.

Towards the aforementioned high level goal, we will need to develop new types of NNs that go beyond the universal function approximation and supervised data [9, 16], and approximate functionals and nonlinear operators instead. As a first step, we resort to a little known but powerful theorem, the *universal operator approximation theorem* [7], which states that a NN with a single hidden layer can approximate accurately any nonlinear continuous *functional* (a mapping from a space of functions into the real numbers) [5, 27, 35] or (nonlinear) operator (a mapping from a space of functions into another space of functions) [7, 6]. To wit, let G be an operator taking an input function u with $G(u)$ the corresponding output function. For any point y in the domain of $G(u)$, the output $G(u)(y)$ is a real number. Hence, the network takes inputs composed of two parts: u and y , and outputs $G(u)(y)$ (Fig. 1A). Although our goal is to learn operators, which take a function as input, we have to represent these input functions discretely, so that network approximations can be applied. We envision that in the future such functions will be represented by other NNs. Here, we explore different representations of the input function, with the simplest one based on the function values at a sufficient but finite number of locations $\{x_1, x_2, \dots, x_m\}$, which we call “sensors” (Fig. 1A). There are other ways to represent a function, e.g. with spectral expansions or as an image, and we demonstrate these in the examples below. In particular, we demonstrate that we can design NNs that can represent accurately both explicit known operators, e.g., integrals, transforms, fractional derivatives and fractional Laplacians, as well as implicit operators known from classical calculus such as nonlinear, deterministic and stochastic ordinary and partial differential equations. The proposed NNs generalizes well, so given unseen functions they predict the action of the operator or predict the solution of the dynamical system accurately.

Materials and Methods

Next, we state the theorem due to Chen & Chen [7] (see Section S1 for more details), based on which we propose the new NN, and subsequently we present data generation and a new theorem that relates the number and type of data with the accuracy of the input functions.

Theorem 1 (Universal Approximation Theorem for Operator). *Suppose that σ is a continuous non-polynomial function, X is a Banach Space, $K_1 \subset X$, $K_2 \subset \mathbb{R}^d$ are two compact sets in X and \mathbb{R}^d , respectively, V is a compact set in $C(K_1)$, G is a nonlinear continuous operator, which maps V into $C(K_2)$. Then for any $\epsilon > 0$, there are positive integers n , p , m , constants*

$c_i^k, \xi_{ij}^k, \theta_i^k, \zeta_k \in \mathbb{R}$, $w_k \in \mathbb{R}^d$, $x_j \in K_1$, $i = 1, \dots, n$, $k = 1, \dots, p$, $j = 1, \dots, m$, such that

$$\left| G(u)(y) - \underbrace{\sum_{k=1}^p \sum_{i=1}^n c_i^k \sigma \left(\sum_{j=1}^m \xi_{ij}^k u(x_j) + \theta_i^k \right)}_{branch} \underbrace{\sigma(w_k \cdot y + \zeta_k)}_{trunk} \right| < \epsilon \quad (1)$$

holds for all $u \in V$ and $y \in K_2$.

This approximation theorem is indicative of the potential application of neural networks to learn nonlinear operators from data, i.e., similar to standard NN where we learn functions from data. However, this theorem does not inform us how to learn operators efficiently. The overall accuracy of NNs can be characterized by dividing the total error into three main types: *approximation*, *optimization*, and *generalization* errors [2, 25, 19, 24]. The universal approximation theorem only guarantees a small approximation error for a sufficiently large network, but it does not consider the important optimization and generalization errors at all, which are often dominant contributions to the total error in practice. Useful networks should be easy to train, i.e., to exhibit small optimization error, and generalize well to unseen data, i.e., to exhibit small generalization error.

To demonstrate the capability and effectiveness of learning nonlinear operators by neural networks, we setup the problem as general as possible by using the weakest possible constraints on the sensors and training dataset. Specifically, the only condition required is that the sensor locations $\{x_1, x_2, \dots, x_m\}$ are the same but not necessarily on a lattice for all input functions u , while we do not enforce any constraints on the output locations y (Fig. 1B). However, even this constraint can be lifted and it is only used here for computational expediency. We propose a specific new network architecture, the deep operator network (DeepONet), to achieve small total errors. We will demonstrate that unlike fully-connected neural networks (FNNs), DeepONet significantly improves generalization based on a design of two sub-networks, the *branch net* for the input function and the *trunk-net* for the locations to evaluate the output function. The key point is that we discover a new operator G as a NN, which is able to make inferences for quantities of interest given new and unseen data. If we wish to further interpret the type of operator G using the familiar classical calculus, we can project the results of $G(u)(y)$ onto a dictionary containing first- or higher-order derivatives, gradients, Laplacians, etc., as it is done currently with existing regression techniques [3, 36]. Returning to the aforementioned example put forward by Gulian et al. [12], using the initial conditions as the function $u(x)$ we can train the operator G offline and then we can predict the dynamics for new unseen boundary conditions with error 10^{-4} or less at a fraction of a second.

We consider two types of implicit operators, i.e., dynamical systems (e.g., in the form of ordinary differential equations, ODEs) and partial differential equations (PDEs). Some works [31, 48] used standard NNs to identify dynamical systems, but they only considered systems described by difference equations. Some other works [29, 34, 33, 11] predict the evolution of a specific dynamical system rather than identifying the system behavior for new unseen input signals. The network architectures they employed includes FNNs [34], recurrent neural networks (RNNs) [29], reservoir computing [29], residual networks [33], autoencoder [11], neural ordinary differential equations [8], and neural jump stochastic differential equations [18]. For identifying PDEs, some works treat the input and output function as an image, and then use convolutional neural networks (CNNs) to learn the image-to-image mapping [43, 49], but this approach can be only applied to the particular type of problems, where the sensors of the input function u are distributed on an equispaced grid, and the training data must include all the $G(u)(y)$ values with y also on an equispaced grid. In another approach without this restriction, PDEs are parameterized by unknown coefficients, and then only

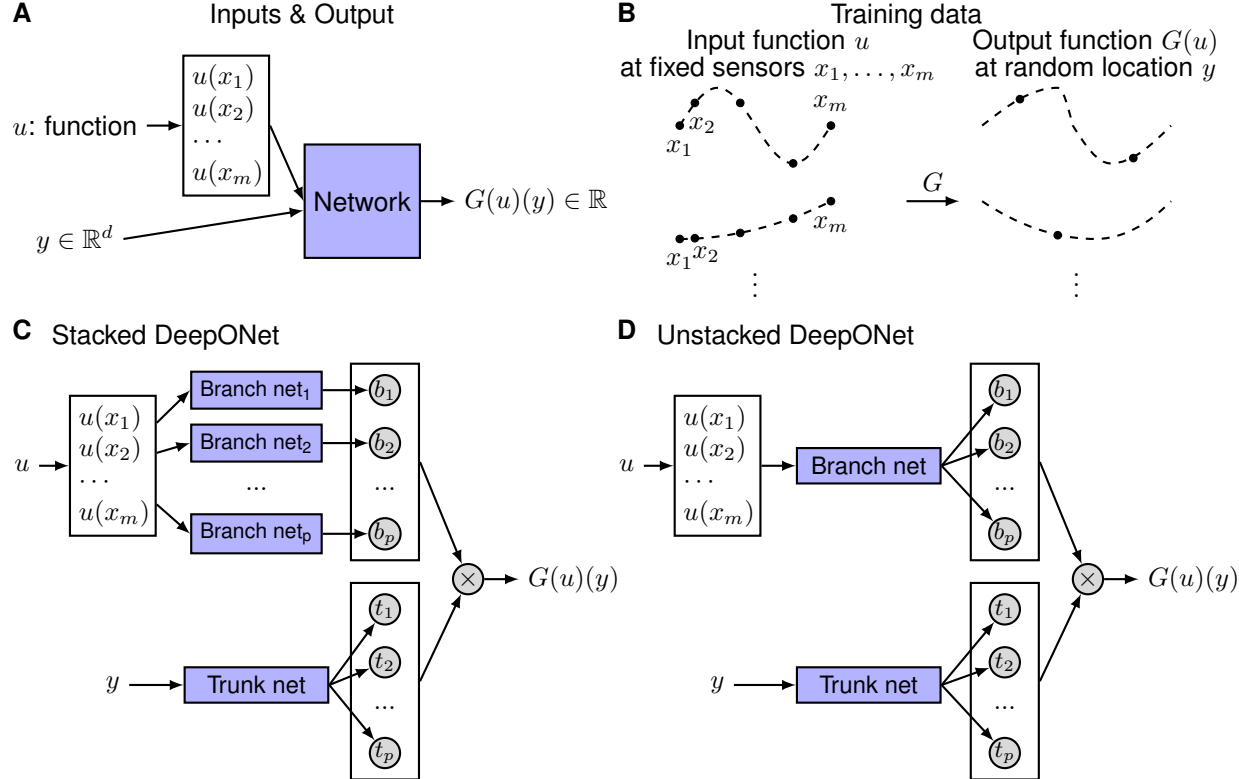


Fig. 1: **A proposal for new architectures that lead to good generalization. Illustrations of the problem setup and architectures of DeepONets.** (A) For the network to learn an operator $G : u \mapsto G(u)$ it takes two inputs $[u(x_1), u(x_2), \dots, u(x_m)]$ and y . (B) Illustration of the training data. For each input function u , we require that we have the same number of evaluations at the same scattered sensors x_1, x_2, \dots, x_m . However, we do not enforce any constraints on the number or locations for the evaluation of output functions. (C) The stacked DeepONet in Theorem 1 has one trunk network and p stacked branch networks. (D) The unstacked DeepONet has one trunk network and one branch network.

the coefficient values are identified from data [3, 36, 45, 30, 23]. Alternatively, a generalized CNN based on generalized moving least squares [40] can be used for unstructured data, but it can only approximate local operators and is not able to learn other operators like an integral operator. In the examples we present below we will explore other representations of the discrete function input space.

DeepONet architecture. We focus on learning operators in a more general setting, where the only requirement for the training dataset is the consistency of the sensors $\{x_1, x_2, \dots, x_m\}$ for input functions. In this general setting, the network inputs consist of two separate components: $[u(x_1), u(x_2), \dots, u(x_m)]^T$ and y (Fig. 1A), and the goal is to achieve good performance by designing the network architecture. One straightforward solution is to directly employ a classical network, such as FNN, CNN or RNN, and concatenate two inputs together as the network input, i.e., $[u(x_1), u(x_2), \dots, u(x_m), y]^T$. However, the input does not have any specific structure, and thus it is not meaningful to choose networks like CNN or RNN; here we use a FNN as the baseline model.

In high dimensional problems, y is a vector with d components, so the dimension of y does not match the dimension of $u(x_i)$ for $i = 1, 2, \dots, m$ any more. This also prevents us from treating $u(x_i)$ and y equally, and thus at least two sub-networks are needed to handle $[u(x_1), u(x_2), \dots, u(x_m)]^T$ and y separately. Although the universal approximation theorem (Theorem 1) does not have any guarantee on the total error, it still provides us with a network structure in Eq. (1). Theorem 1 only considers a shallow network with one hidden layer, so we extend it to deep networks to gain expressivity. The architecture we propose is shown in Fig. 1C. First there is a “trunk” network, which takes y as the input and outputs $[t_1, t_2, \dots, t_p]^T \in \mathbb{R}^p$. In addition to the trunk network, there are p “branch” networks, and each of them takes $[u(x_1), u(x_2), \dots, u(x_m)]^T$ as the input and outputs a scalar $b_k \in \mathbb{R}$ for $k = 1, 2, \dots, p$. We merge them together as in Eq. (1): $G(u)(y) \approx \sum_{k=1}^p b_k t_k$. We note that the trunk network also applies activation functions in the last layer, i.e., $t_k = \sigma(\cdot)$ for $k = 1, 2, \dots, p$, and thus this trunk-branch network can also be seen as a trunk network with each weight in the last layer parameterized by another branch network instead of the classical single variable. We also note that in Eq. (1) the last layer of each b_k branch network does not have bias. Although bias is not included in Theorem 1, adding bias may increase the performance by reducing the generalization error. In addition to adding bias to the branch networks, we also add a bias $b_0 \in \mathbb{R}$ in the last stage: $G(u)(y) \approx \sum_{k=1}^p b_k t_k + b_0$.

In practice, p is at least of the order of 10, and using lots of branch networks is inefficient. Hence, we merge all the branch networks into one single branch network (Fig. 1D), i.e., a single branch network outputs a vector $[b_1, b_2, \dots, b_p]^T \in \mathbb{R}^p$. In the first DeepONet (Fig. 1C), there are p branch networks stacked parallel, so we name it “stacked DeepONet”, while we refer to the second DeepONet (Fig. 1D) as “unstacked DeepONet”. All versions of DeepONets are implemented in DeepXDE [23], a user-friendly Python library designed for scientific machine learning. The loss function we used is the mean squared error (MSE) between the true value of $G(u)(y)$ and the network prediction for the input $([u(x_1), u(x_2), \dots, u(x_m)], y)$.

DeepONet is a high-level network architecture without defining the architectures of its inner trunk and branch networks. To demonstrate the capability and good performance of DeepONet alone, we choose the simplest FNN as the architectures of the sub-networks in this study. It is possible that using convolutional layers we could further improve accuracy. However, convolutional layers usually work for square domains with $\{x_1, x_2, \dots, x_m\}$ on a equispaced grid, so as alternative and for a more general setting we may use the “attention” mechanism [41].

Embodying some prior knowledge into neural network architectures usually induces good generalization. This inductive bias has been reflected in many networks, such as CNN for images and

RNN for sequential data. The success of DeepONet even using FNN as its sub-networks is also due to its strong inductive bias. The output $G(u)(y)$ has two independent inputs u and y , and thus using the trunk and branch networks explicitly is consistent with this prior knowledge. More broadly, $G(u)(y)$ can be viewed as a function of y conditioning on u . Finding an effective way to represent the conditioning input is still an open question, and different approaches have been proposed, such as feature-wise transformations [10].

Data generation. The input function $u(x)$ plays an important role in operator identification; in this study, we mainly consider the following function spaces: Gaussian random fields (GRF), spectral representations, and formulating the input functions as images; more details are given in Section S2.

In order to estimate how many sensors are required to achieve accuracy ε , we consider the following ODE system:

$$\text{Problem 1} \quad \begin{cases} \frac{d}{dx} \mathbf{s}(x) = \mathbf{g}(\mathbf{s}(x), u(x), x) \\ \mathbf{s}(a) = \mathbf{s}_0 \end{cases}, \quad (2)$$

where $u \in V$ (a compact subset of $C[a, b]$) is the input signal, and $\mathbf{s} : [a, b] \rightarrow \mathbb{R}^K$ is the solution of system (2) serving as the output signal.

Let G be the operator mapping the input u to the output \mathbf{s} , i.e., $G(u)$ satisfies

$$G(u)(x) = \mathbf{s}_0 + \int_a^x \mathbf{g}(G(u)(t), u(t), t) dt.$$

Now, we choose uniformly $m + 1$ points $x_j = a + j(b - a)/m, j = 0, 1, \dots, m$ from $[a, b]$, and define the function $u_m(x)$ as follows:

$$u_m(x) = u(x_j) + \frac{u(x_{j+1}) - u(x_j)}{x_{j+1} - x_j} (x - x_j), \quad x_j \leq x \leq x_{j+1}, \quad j = 0, 1, \dots, m - 1.$$

Denote the operator mapping u to u_m by \mathcal{L}_m , and let $U_m = \{\mathcal{L}_m(u) | u \in V\}$, which is a compact subset of $C[a, b]$, since V is compact and continuous operator \mathcal{L}_m keeps the compactness. Obviously, $W_m := V \cup U_m$ as the union of two compact sets is also compact. Then, set $W := \bigcup_{i=1}^{\infty} W_i$, and the Lemma in Section S4 points out that W is still a compact set. Since G is a continuous operator, $G(W)$ is compact in $C([a, b]; \mathbb{R}^K)$. For convenience of analysis, we assume that $\mathbf{g}(\mathbf{s}, u, x)$ satisfies the Lipschitz condition with respect to \mathbf{s} and u on $G(W) \times W$, i.e., there is a constant $c > 0$ such that

$$\begin{aligned} \|\mathbf{g}(\mathbf{s}_1, u, x) - \mathbf{g}(\mathbf{s}_2, u, x)\|_2 &\leq c\|\mathbf{s}_1 - \mathbf{s}_2\|_2 \\ \|\mathbf{g}(\mathbf{s}, u_1, x) - \mathbf{g}(\mathbf{s}, u_2, x)\|_2 &\leq c|u_1 - u_2|. \end{aligned}$$

Note that this condition is easy to achieve, for instance, as long as \mathbf{g} is differentiable with respect to \mathbf{s} and u on $G(W) \times W$.

For $u \in V, u_m \in U_m$, there exists a constant $\kappa(m, V)$ depending on m and compact space V , such that

$$\max_{x \in [a, b]} |u(x) - u_m(x)| \leq \kappa(m, V), \quad \kappa(m, V) \rightarrow 0 \text{ as } m \rightarrow \infty. \quad (3)$$

When V is GRF with the Gaussian kernel, we have $\kappa(m, V) \sim \frac{1}{m^2 l^2}$, see Section S3 for the proof. Based on the these concepts, we have the following theorem.

Theorem 2. Suppose that m is a positive integer making $c(b-a)\kappa(m, V)e^{c(b-a)}$ less than ε , then for any $d \in [a, b]$, there exist $\mathcal{W}_1 \in \mathbb{R}^{n \times (m+1)}$, $b_1 \in \mathbb{R}^{m+1}$, $\mathcal{W}_2 \in \mathbb{R}^{K \times n}$, $b_2 \in \mathbb{R}^K$, such that

$$\|G(u)(d) - (\mathcal{W}_2 \cdot \sigma(\mathcal{W}_1 \cdot [u(x_0) \quad \cdots \quad u(x_m)]^T + b_1) + b_2)\|_2 < \varepsilon$$

holds for all $u \in V$.

Proof. The proof can be found in Section S4. \square

Results and Discussion

We first show how to learn explicit operators, e.g., integration, fractional derivative and the 2D fractional Laplacian, and demonstrate small generalization error for different representations of the discrete input space V . We then present how to learn implicit operators, including a deterministic PDE and two stochastic differential equations. The parameter values for all examples are listed in Section S5, and the verification of the Hölder continuity of all the explicit and implicit operators considered in this study is shown in Section S13.

Learning explicit operators. First, we consider a pedagogical example described by

$$\frac{ds(x)}{dx} = g(s(x), u(x), x), \quad x \in (0, 1],$$

with an initial condition (IC) $s(0) = 0$. Our goal is to predict $s(x)$ over the whole domain $[0, 1]$ for any $u(x)$. We first consider a linear problem by choosing $g(s(x), u(x), x) = u(x)$, which is equivalent to learning the antiderivative operator. That is,

$$\textbf{Problem 1.A} \quad \frac{ds(x)}{dx} = u(x), \quad \text{and} \quad G : u(x) \mapsto s(x) = s_0 + \int_0^x u(\tau) d\tau, \quad x \in [0, 1]. \quad (4)$$

We train FNNs and residual neural networks (ResNets) [15] to learn the antiderivative operator. To obtain the best performance of FNNs, we grid search the three hyperparameters: depth from 2 to 4, width from 10 to 2560, and learning rate from 0.0001 to 0.01. The mean squared errors (MSE) of the test dataset with learning rate 0.01, 0.001, and 0.0001 are shown in Fig. S1. Although we only choose depth up to 4, the results show that increasing the depth further does not improve the test error. Among all these hyperparameters, the smallest test error $\sim 7 \times 10^{-5}$ is obtained for the network with depth 2, width 2560, and learning rate 0.001. We observe that when the network is small, the training error is large and the generalization error (the difference between test error and training error) is small, due to small expressivity. When the network size increases, the training error decreases, but the generalization error increases. We stop the training before FNNs reach the overfitting region, where the test error increases. Similarly, for ResNets, we grid search the two hyperparameters: the number of residual blocks from 1 to 5, and width from 10 to 320. We note that one residual block includes two dense layers with a shortcut connection, and each ResNet has one hidden layer before the first residual block and one hidden layer after the last residual block [15], and thus a ResNet has in total (3+2# residual block) layers. We choose the learning rate as 0.001 based on the previous results of FNNs. Among all these hyperparameters, the smallest test error $\sim 1 \times 10^{-4}$ is obtained for the ResNet with 1 residual block and width 20.

Compared to FNNs and ResNets, DeepONets have much smaller generalization error and thus smaller test error. Here we do not aim to find the best hyperparameters, and only test the performance of the two DeepONets listed Table S3. The training trajectory of an unstacked DeepONet

with bias is shown in Fig. 2B, and the generalization error is negligible. We observe that for both stacked and unstacked DeepONets, adding bias to branch networks reduces both training and test errors (Fig. 2A); DeepONets with bias also have smaller uncertainty, i.e., they are more stable for training from random initialization (Fig. 2A). Compared to stacked DeepONets, although unstacked DeepONets have larger training error, the test error is smaller, due to the smaller generalization error. Therefore, unstacked DeepONets with bias achieve the best performance. In addition, unstacked DeepONets have fewer number of parameters than stacked DeepONets, and thus can be trained faster using much less memory. We also provide the examples of Legendre transform in Section S6 and nonlinear ODE in Section S7 with more details on the accuracy and architecture. In the following study, we will use unstacked DeepONets.

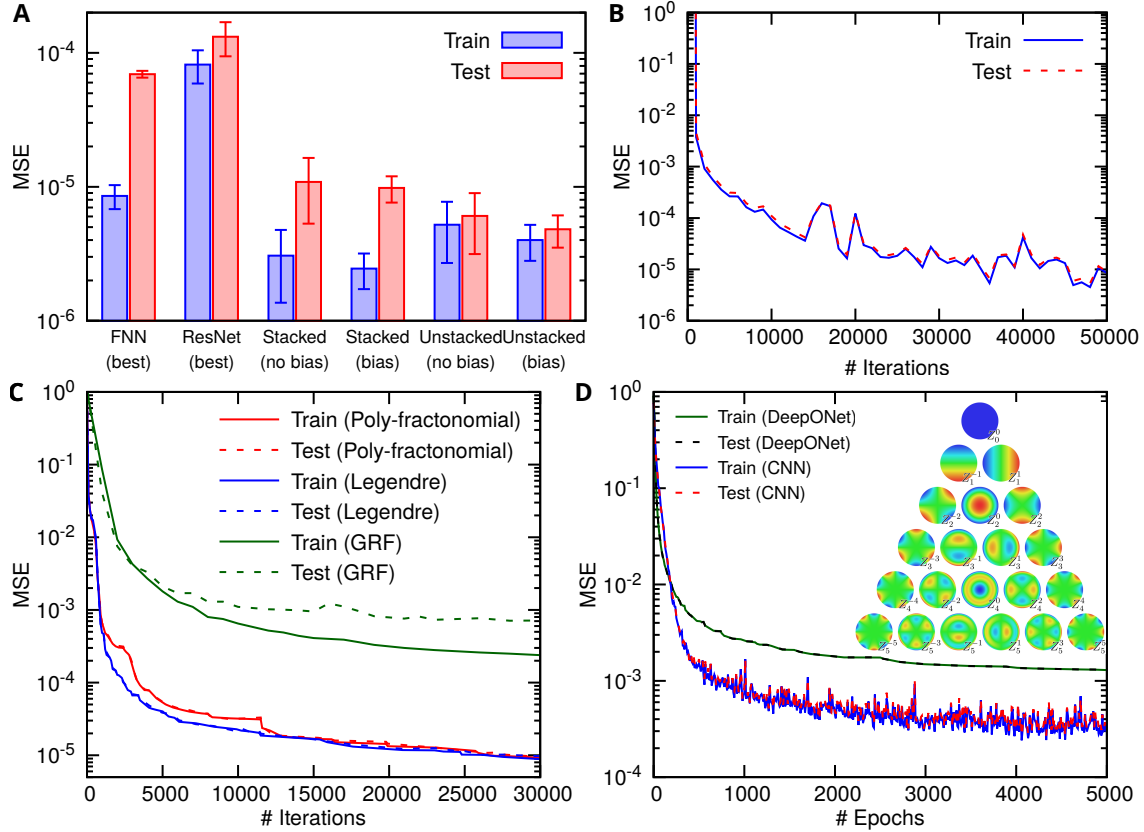


Fig. 2: Learning explicit Operators using different V spaces and different architectures. Top row: Effect of architectures. Errors of DeepONets trained to learn the antiderivative operator (linear case). **(A)** The training/test errors of stacked/unstacked DeepONets with/without bias compared to the best test error and the corresponding training error of FNNs and ResNets. The error bars are the one-standard-deviation from 10 runs with different training/test data and network initialization. **(B)** The training trajectory of an unstacked DeepONet with bias. Lower row: Effect of space V . **(C)** learning the Caputo fractional derivative: poly-fractonomials vs Legendre vs GRF. **(D)** Learning the fractional Laplacian on a disk. The V space consists of the Zernike polynomials.

In addition to the aforementioned integral operator, we consider integro-differential operators, namely, fractional differential operators, in order to demonstrate the flexibility of DeepONets to learn more complicated operators. The first fractional differential operator we learn is the 1D

Caputo fractional derivative [32]:

$$\textbf{Problem 2} \quad G(u)(y, \alpha) : u(x) \mapsto s(y, \alpha) = \frac{1}{\Gamma(1-\alpha)} \int_0^y (y-\tau)^{-\alpha} u'(\tau) d\tau, \quad y \in [0, 1], \alpha \in (0, 1),$$

where α and $u'(\cdot)$ are the fractional order and first derivative of u , respectively. The domain of output function now includes two variables y and α . We concatenate y and α to form an augmented $\hat{y} = [y, \alpha]^T$ and then feed \hat{y} to the trunk net. We consider the influence of different V spaces on the generalization error of DeepONets. These spaces include two orthogonal polynomial spaces spanned by poly-factonomials [44] and Legendre polynomials, as well as the GRF. More details can be found in Section S12. Fig. 2C shows the generalization errors for the three different V spaces. We see that small generalization errors are achieved for all of the cases. The generalization error for GRF is slightly larger than those for orthogonal polynomial spaces, since for GPR we select different characteristic lengths l 's in the RBF kernel for training and test sets.

The second fractional differential operator we learn is the 2D Riesz fractional Laplacian [22]:

$$\textbf{Problem 3} \quad G(u)(y, \alpha) : u(x) \mapsto s(y, \alpha) = \frac{2^\alpha \Gamma(1 + \frac{\alpha}{2})}{\pi |\Gamma(-\frac{\alpha}{2})|} \times \text{p.v.} \int_{\mathbb{R}^2} \frac{u(y) - u(\tau)}{\|y - \tau\|_2^{2+\alpha}} d\tau, \quad \alpha \in (0, 2),$$

where “p.v.” means principle value. The input and out functions are both assumed to be identically zero outside of a unit disk centered at the origin. The 2D fractional Laplacian reduces to standard Laplacian Δ as the fractional order α goes to two. For learning this operator, we specify the V space to be the orthogonal space spanned by the Zernike polynomials [1], which are commonly used to generate or approximate functions defined on a unit disk. Fig. 2D (inset) displays the first 21 Zernike polynomials; see a more detailed description of the polynomial expansions in Section S2. Importantly, we consider two different NN architectures: trunk and unstacked branch nets versus CNNs. For the first architecture, in a similar manner for handling the 1D Caputo derivative case, we feed the augmented $\hat{y} = [y, \alpha]$ to the trunk net. For the CNN architecture, we rearrange the values of input and output functions to 2D images in which “pixel” (or function) values are attached to a lattice in the polar coordinate. We first utilize a CNN as an encoder to extract the features of the input image, which reduces the high-dimensional input space to a low-dimensional latent space, and then we employ another CNN as a decoder to map the vector in the latent space to the output space. To accommodate the extra parameter α , we set the image consisting of values of $G(y, \alpha_k)$ for k -th α as the k -th channel of the output image. As such, we obtain a multi-channel output image. We observe from Fig. 2D that both architectures yield small generalization errors. Moreover, the CNN architecture gains slightly higher operator approximation accuracy than the branch-trunk nets. This is because the former sufficiently takes advantage of the spatial structure of the training data. Nevertheless, DeepONet is more flexible than CNN for unstructured data as we commented in preceding paragraphs. More details are shown in Section S12.

DeepONet learns fast. An important question for the effectiveness of DeepONet is how fast it learns new operators. We investigate this question by learning a system of ODEs first and subsequently a nonlinear PDE. First, we consider the motion of a gravity pendulum with an external force described by

$$\textbf{Problem 1.B} \quad \frac{ds_1}{dt} = s_2, \quad \frac{ds_2}{dt} = -k \sin s_1 + u(t),$$

with an initial condition $s(0) = \mathbf{0}$, and k determined by the acceleration due to gravity and the length of the pendulum. This problem is characterized by three factors: (1) k , (2) maximum

prediction time T , and (3) input function space. The accuracy of learned networks is determined by four factors: (1) the number of sensor points m ; (2) training dataset size; (3) network architecture, (4) optimizer. We investigate the effects of all these factors on the accuracy of DeepONet in Section S8 and verify our analysis on the number of sensors, but here we focus on the convergence rate of the training process.

The test and generalization errors of networks with different width are shown in Fig. 3. It is surprising that the test and generalization errors have exponential convergence for small training dataset size. Even for a large dataset, the polynomial convergence rates are still higher than the classical $x^{-0.5}$ in the learning theory [28]. This fast convergence reveals that DeepONets learn exponentially fast, especially in the region of small dataset. Moreover, the transition point from exponential to polynomial convergence depends on the network size, and a larger exponential regime can be accomplished with a sufficiently large network.

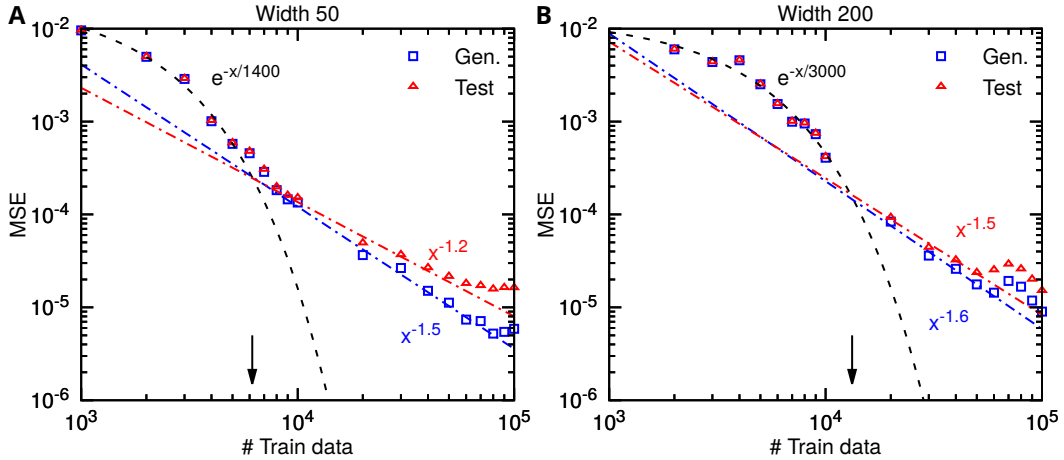


Fig. 3: **Fast learning of implicit operators – a nonlinear pendulum.** Initial exponential decay of test/generalization error. The range of exponential convergence increases with the size of the neural network. The test and generalization errors have exponential convergence for small training datasets, and then converge with polynomial rates. The transition point from exponential to polynomial (indicated by the arrow) convergence depends on the width, and a bigger network has a later transition point.

Next, we learn an implicit operator in the form of a nonlinear diffusion-reaction PDE with a source term $u(x)$ described by

$$\text{Problem 4} \quad \frac{\partial s}{\partial t} = D \frac{\partial^2 s}{\partial x^2} + ks^2 + u(x), \quad x \in (0, 1), t \in (0, 1],$$

with zero initial/boundary conditions, where $D = 0.01$ is the diffusion coefficient, and $k = 0.01$ is the reaction rate. We use DeepONets to learn the operator mapping from $u(x)$ to the PDE solution $s(x, t)$. In the previous examples, for each input u , we only use one random point of $s(x)$ for training, and instead we may also use multiple points of $s(x)$. To generate the training dataset, we solve the diffusion-reaction system using a second-order implicit finite difference method on a 100 by 100 grid, and then for each s we randomly select P points out of these 10000 ($= 100 \times 100$) grid points (Fig. S8). Hence, the dataset size is equal to the product of P by the number of u samples. We confirm that the training and test datasets do not include the data from the same s .

We investigate the error tendency with respect to the number of u samples and the value of P . When we use 100 random u samples, the test error decreases first as P increases (Fig. 4A),

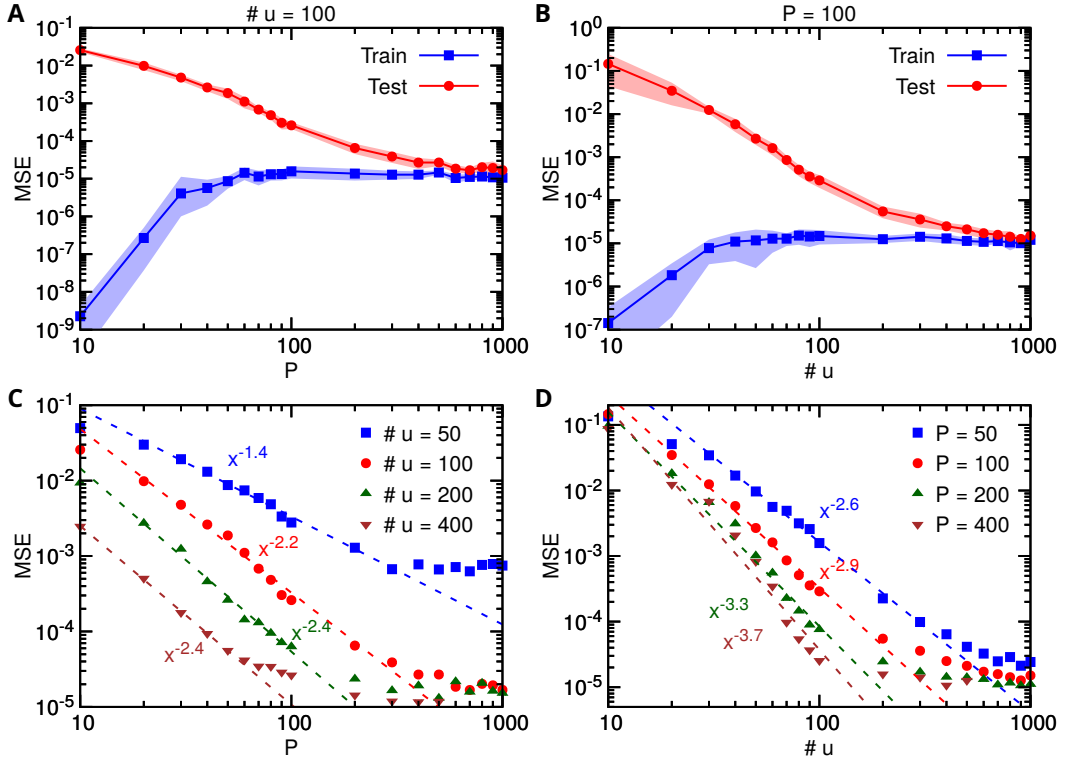


Fig. 4: **Fast Learning of implicit operators – a diffusion-reaction system.** **Top-row:** Comparison of training and testing errors. Learning a diffusion-reaction system. **(A)** Training error (blue) and test error (red) for different values of the number of random points P when 100 random u samples are used. **(B)** Training error (blue) and test error (red) for different number of u samples when $P = 100$. The shaded regions denote one-standard-deviation. **Lower row:** Learning a reaction-diffusion system. The initial decay is exponential ($P, u < 50$) and the int transitions to algebraic decay in terms of the P sampling point in $x - t$ domain and the excitation function $u(x, t)$. Error convergence rates for different number of training data points. **(C)** Convergence of test error with respect to P for different number of u samples. **(D)** Convergence of test error with respect to the number of u samples for different values of P .

and then saturates due to other factors, such as the finite number of u samples and fixed neural network size. We observe a similar error tendency but with less saturation as the number of u samples increases with P fixed (Fig. 4B). In addition, in this PDE problem the DeepONet is able to learn from a small dataset, e.g., a DeepONet can reach the test error of $\sim 10^{-5}$ when it is only trained with 100 u samples ($P = 1000$). We recall that we test on 10000 grid points, and thus on average each location point only has $100 \times 1000/10000 = 10$ training data points. For comparison, we train ResNets of different sizes with the same setup, and the test error is of $\sim 10^{-1}$ due to large generalization error (Table S4).

Before the error saturates, the rates of convergence with respect to both P and the number of u samples obey a polynomial law in most of the range (Figs. 4C and D). The rate of convergence versus P depends on the number of u samples, and more u samples induce faster convergence until saturation (see the blue line in Fig. S9D). Similarly, the rate of convergence versus the number of u samples depends on the value of P (see, the red line in Fig. S9D). In addition, in the initial range of the convergence, we observe an exponential convergence (see Figs. S9A and B). The coefficient $1/k$ in the exponential convergence $e^{-x/k}$ also depends on the number of u samples or the value of P (see Fig. S9C). It is reasonable that the convergence rate presented in Figs. S9C and D increases with the number of u samples or the value of P , because the total number of training data points is equal to $P \times \#u$. However, by fitting the points, it is surprising that there is a clear tendency in the form of either $\ln(x)$ or e^{-x} (Figs. S9C and D), which we cannot fully explain yet, and hence more theoretical and computational investigations are required. We also provide the examples of advection equation in Section S10 and advection-diffusion equation in Section S11.

Learning stochastic operators. Next, we demonstrate that we can learn high-dimensional operators, so here we consider a stochastic ODE and a stochastic PDE and present our main findings.

Consider the population growth model

$$\textbf{Problem 5} \quad dy(t; \omega) = k(t; \omega)y(t; \omega)dt, \quad t \in (0, 1] \text{ and } \omega \in \Omega, \quad (5)$$

with $y(0) = 1$. Here Ω is the random space. The randomness comes from the coefficient $k(t; \omega)$; here, $k(t; \omega)$ is modeled as a Gaussian random process such that

$$k(t; \omega) \sim \mathcal{GP}(k_0(t), \text{Cov}(t_1, t_2)),$$

where the mean $k_0(t) = 0$ and the covariance function is $\text{Cov}(t_1, t_2) = \sigma^2 \exp(-\|t_1 - t_2\|^2/2l^2)$. We choose $\sigma = 1$, and the correlation length l is in the range $[1, 2]$.

We use DeepONet to learn the operator mapping from $k(t; \omega)$ of different correlation lengths to the solution $y(t; \omega)$. We note that we do not assume we know the covariance function for training DeepONet. The main differences between this example and the previous examples are that 1) here the input of the branch net is a random process instead of a function, 2) the input of the trunk net contains both physical spaces and random spaces. Specifically, to handle the random process as the input, we employ the Karhunen-Loeve (KL) expansion,

$$k(t; \omega) \approx \sum_{i=1}^N \sqrt{\lambda_i} e_i(t) \xi_i(\omega),$$

where N is the number of retained modes, λ_i and $e_i(t)$ are the i -th largest eigenvalue and its associated normalized eigenfunction of the covariance function, respectively, and ξ_1, \dots, ξ_N are

independent standard Gaussian random variables. Then the input of the branch net is the N eigenfunctions scaled by the eigenvalues

$$[\sqrt{\lambda_1}e_1(t), \sqrt{\lambda_2}e_2(t), \dots, \sqrt{\lambda_N}e_N(t)] \in \mathbb{R}^{N \times m},$$

where $\sqrt{\lambda_i}e_i(t) = \sqrt{\lambda_i}[(e_i(t_1), e_i(t_2), \dots, e_i(t_m))] \in \mathbb{R}^m$, and the input of the trunk net is $[t, \xi_1, \xi_2, \dots, \xi_N] \in \mathbb{R}^{N+1}$.

We choose $N = 5$, which is sufficient to conserve 99.9% stochastic energy. We train a DeepONet with a dataset of 10000 different $k(t; \omega)$ with l randomly sampled in $[1, 2]$, and for each $k(t; \omega)$ we use only one realization. The test MSE is $8.0 \times 10^{-5} \pm 3.4 \times 10^{-5}$, and as an example the prediction for 10 different random samples from $k(t; \omega)$ with $l = 1.5$ is in Fig. 5.

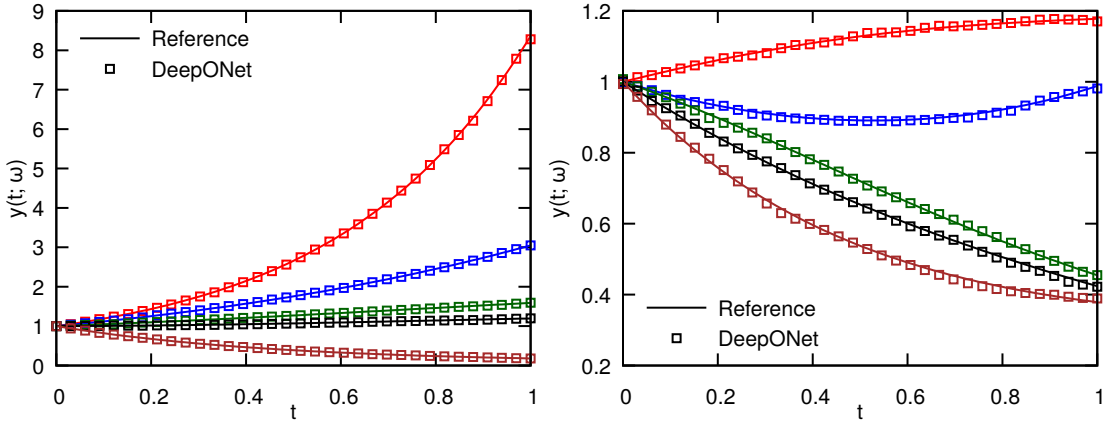


Fig. 5: **DeepONet prediction for a stochastic ODE.** The DeepONet prediction (dots) is very close to the reference solution for 10 different random samples from $b(x; \omega)$ with $l = 1.5$.

Next, we consider the following elliptic problem with multiplicative noise

$$\textbf{Problem 6} \quad -\operatorname{div}(e^{b(x; \omega)} \nabla u(x; \omega)) = f(x), \quad x \in (0, 1) \text{ and } \omega \in \Omega,$$

with Dirichlet boundary conditions $u(0) = u(1) = 0$. The randomness comes from the diffusion coefficient $e^{b(x; \omega)}$, and $b(x; \omega) \sim \mathcal{GP}(b_0(x), \operatorname{Cov}(x_1, x_2))$, where the mean $b_0(x) = 0$ and the covariance function is $\operatorname{Cov}(x_1, x_2) = \sigma^2 \exp(-\|x_1 - x_2\|^2/2l^2)$. In this example, we choose a constant forcing term $f(x) = 10$, and we set the standard deviation $\sigma = 0.1$ and correlation length in the range $[1, 2]$.

We use DeepONet to learn the operator mapping from $b(x; \omega)$ of different correlation lengths to the solution $u(x; \omega)$. We train a DeepONet with a dataset of 10000 different $b(x; \omega)$ with l randomly sampled in $[1, 2]$, and for each $b(x, \omega)$ we use only one realization. The test MSE is $2.0 \times 10^{-3} \pm 1.7 \times 10^{-3}$, and as an example the prediction for 10 different random samples from $b(x; \omega)$ with $l = 1.5$ is in Fig. 6. We have a relative larger error in this stochastic elliptic problem, and to reduce the error further, we can remove outliers of the random variables $\{\xi_1, \xi_2, \dots, \xi_N\}$ by clipping them to a bounded domain. For instance, if the random variables are clipped to $[-3.1, 3.1]$, which is sufficient large to keep 99% probability space, then the test MSE is reduced to $9.4 \times 10^{-4} \pm 3.0 \times 10^{-4}$.

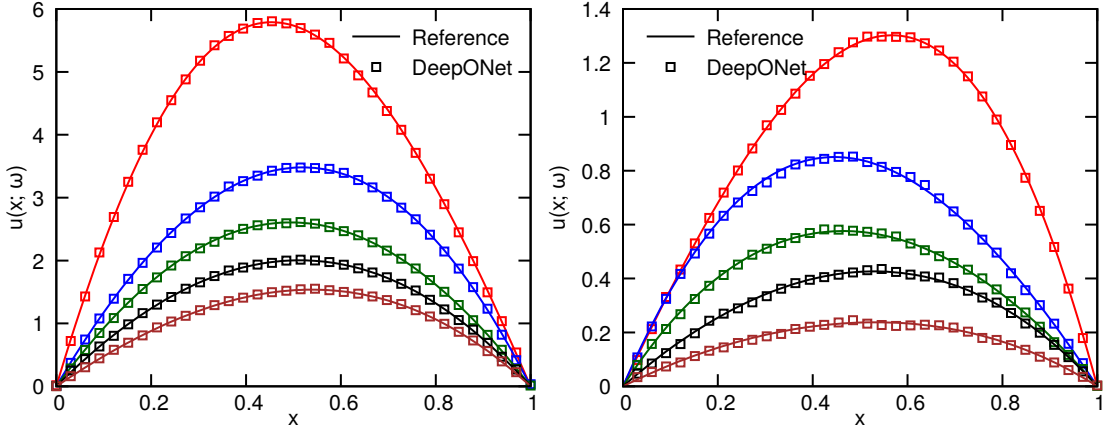


Fig. 6: **DeepONet prediction for a stochastic elliptic equation.** The DeepONet prediction (dots) is very close to the reference solution for 10 different random samples from $b(x; \omega)$ with $l = 1.5$.

Conclusion

We have formulated, for first time, the problem of learning operators in a general setup, and proposed DeepONets to learn linear and nonlinear explicit and implicit operators. In DeepONets, we first construct two sub-networks to encode input functions and location variables separately, and then merge them together to compute the output. We test DeepONets on learning explicit operators, including fractional operators, as well as implicit operators in the form of deterministic and stochastic ordinary/partial differential equations. Our two main findings are that the generalization error is small, and that the training and testing errors decay fast with respect to the training data size. In fact, we observed exponential fast learning for sufficiently large networks and transition to standard convergence for large data sets. It is conceivable that a different type of architecture, a much bigger size or a different type could maintain exponential fast learning for much bigger data sizes. In our simulations, we studied systematically the effects on the test error of different factors, including the number of sensors, maximum prediction time, the complexity of the space of input functions, training dataset size, and network size. Moreover, we derived theoretically the dependence of approximation error on different factors, which is consistent with our computational results.

Despite the reported progress in this first paper, more work should be done both theoretically and computationally. Training DeepONet is much more computationally intensive than training standard NNs for function approximation, and hence more research is needed in speeding up the training process and in formulating efficient offline training strategies, including perhaps transfer learning approaches. Here, we have employed known operators in order to evaluate the accuracy of DeepONet systematically, however, the real strength of DeepONet is that it can discover new operators that are trained by multi-fidelity data or by heterogeneous sources of experimental data and simulation data. We could also endow the operator G with prior knowledge, e.g. translational and rotational invariances as in CNN for imaging [38]. On the theoretical side, there have not been any results on the network size for operator approximation, similar to the bounds of width and depth for function approximation [13]. We also do not understand theoretically yet why DeepONets can induce small generalization errors. On the other hand, in this paper we use fully-connected neural networks for the two sub-networks, but as we discussed in Materials and Methods, we can

also employ other network architectures, such as convolutional neural networks or the “attention” mechanism. These modifications may improve further the accuracy of DeepONets, and the example of using CNN with encoders and decoders for learning the fractional Laplacian presented here is a first such indication.

In summary, we have formulated a new framework to learn linear and nonlinear operators implicitly as NNs. In theory, all the operators of the classical integer calculus but also of fractional calculus can be represented by carefully trained NNs as well as other transforms and even theorems, e.g. the Gauss theorem. An even more exciting prospect is to use the big data available in social media to discover new operators that will quantify the currently unknown laws of social dynamics.

Acknowledgments

We thank Yanhui Su of Fuzhou University for helpful discussions. This work is supported by the DOE PhILMs project (No. DE-SC0019453) and the DARPA-AIRA grant HR00111990025. The work of Pengzhan Jin is partially supported by the Major Project on New Generation of Artificial Intelligence from the Ministry of Science and Technology of China (Grant No. 2018AAA010100).

Author contributions

L.L. and G.E.K. designed the study based on G.E.K’s original idea. L.L. developed DeepONet architectures. L.L., P.J. and Z.Z. developed the theory. L.L. performed the experiments of the integral, nonlinear ODE, gravity pendulum, and stochastic ODE/PDE operators. L.L. and P.J. performed the experiments of the Legendre transform, diffusion-reaction, advection, and advection-diffusion PDEs. G.P. performed the experiments of fractional operators. L.L., P.J., G.P., Z.Z. and G.E.K. wrote the manuscript. G.E.K. supervised the project.

Competing interests statement

The authors declare that they have no competing interests.

References

- [1] M. Born and E. Wolf. *Principles of optics: electromagnetic theory of propagation, interference and diffraction of light*. Elsevier, 2013.
- [2] L. Bottou and O. Bousquet. The tradeoffs of large scale learning. In *Advances in Neural Information Processing Systems*, pages 161–168, 2008.
- [3] S. L. Brunton, J. L. Proctor, and J. N. Kutz. Discovering governing equations from data by sparse identification of nonlinear dynamical systems. *Proceedings of the National Academy of Sciences*, 113(15):3932–3937, 2016.
- [4] J. Charrier. Strong and weak error estimates for elliptic partial differential equations with random coefficients. *SIAM Journal on Numerical Analysis*, 50(1):216–246, 2012.
- [5] T. Chen and H. Chen. Approximations of continuous functionals by neural networks with application to dynamic systems. *IEEE Transactions on Neural Networks*, 4(6):910–918, 1993.

- [6] T. Chen and H. Chen. Approximation capability to functions of several variables, nonlinear functionals, and operators by radial basis function neural networks. *IEEE Transactions on Neural Networks*, 6(4):904–910, 1995.
- [7] T. Chen and H. Chen. Universal approximation to nonlinear operators by neural networks with arbitrary activation functions and its application to dynamical systems. *IEEE Transactions on Neural Networks*, 6(4):911–917, 1995.
- [8] T. Q. Chen, Y. Rubanova, J. Bettencourt, and D. K. Duvenaud. Neural ordinary differential equations. In *Advances in Neural Information Processing Systems*, pages 6571–6583, 2018.
- [9] G. Cybenko. Approximation by superpositions of a sigmoidal function. *Mathematics of Control, Signals and Systems*, 2(4):303–314, 1989.
- [10] V. Dumoulin, E. Perez, N. Schucher, F. Strub, H. d. Vries, A. Courville, and Y. Bengio. Feature-wise transformations. *Distill*, 2018. <https://distill.pub/2018/feature-wise-transformations>.
- [11] N. B. Erichson, M. Muehlebach, and M. W. Mahoney. Physics-informed autoencoders for Lyapunov-stable fluid flow prediction. *arXiv preprint arXiv:1905.10866*, 2019.
- [12] M. Gulian, M. Raissi, P. Perdikaris, and G. Karniadakis. Machine learning of space-fractional differential equations. *SIAM Journal on Scientific Computing*, 41(4):A2485–A2509, 2019.
- [13] B. Hanin. Universal function approximation by deep neural nets with bounded width and ReLU activations. *arXiv preprint arXiv:1708.02691*, 2017.
- [14] Z. Hao, H. Li, Z. Zhang, and Z. Zhang. Sharp error estimates of a spectral Galerkin method for a diffusion-reaction equation with integral fractional Laplacian on a disk. *Submitted*, 2019. <https://www.researchgate.net/publication/335892990>.
- [15] K. He, X. Zhang, S. Ren, and J. Sun. Deep residual learning for image recognition. In *Proceedings of the IEEE Conference on Computer Vision and Pattern Recognition*, pages 770–778, 2016.
- [16] K. Hornik, M. Stinchcombe, and H. White. Multilayer feedforward networks are universal approximators. *Neural Networks*, 2(5):359–366, 1989.
- [17] R. Iten, T. Metger, H. Wilming, L. Del Rio, and R. Renner. Discovering physical concepts with neural networks. *arXiv preprint arXiv:1807.10300*, 2018.
- [18] J. Jia and A. R. Benson. Neural jump stochastic differential equations. *arXiv preprint arXiv:1905.10403*, 2019.
- [19] P. Jin, L. Lu, Y. Tang, and G. E. Karniadakis. Quantifying the generalization error in deep learning in terms of data distribution and neural network smoothness. *arXiv preprint arXiv:1905.11427*, 2019.
- [20] D. P. Kingma and J. Ba. Adam: A method for stochastic optimization. *arXiv preprint arXiv:1412.6980*, 2014.
- [21] O. A. Ladyženskaja, V. A. Solonnikov, and N. N. Ural’ceva. *Linear and quasilinear equations of parabolic type*. AMS, Providence, R.I., 1968.

[22] A. Lischke, G. Pang, M. Gulian, F. Song, C. Glusa, X. Zheng, Z. Mao, W. Cai, M. M. Meerschaert, M. Ainsworth, et al. What is the fractional Laplacian? a comparative review with new results. *Journal of Computational Physics*, 404:109009, 2020.

[23] L. Lu, X. Meng, Z. Mao, and G. E. Karniadakis. DeepXDE: A deep learning library for solving differential equations. *arXiv preprint arXiv:1907.04502*, 2019.

[24] L. Lu, Y. Shin, Y. Su, and G. E. Karniadakis. Dying ReLU and initialization: Theory and numerical examples. *arXiv preprint arXiv:1903.06733*, 2019.

[25] L. Lu, Y. Su, and G. E. Karniadakis. Collapse of deep and narrow neural nets. *arXiv preprint arXiv:1808.04947*, 2018.

[26] M. M. Meerschaert, J. Mortensen, and H.-P. Scheffler. Vector grunwald formula for fractional derivatives. *Fractional Calculus and Applied Analysis*, 7(1):61–82, 2004.

[27] H. N. Mhaskar and N. Hahm. Neural networks for functional approximation and system identification. *Neural Computation*, 9(1):143–159, 1997.

[28] M. Mitzenmacher and E. Upfal. *Probability and computing: randomization and probabilistic techniques in algorithms and data analysis*. Cambridge University Press, 2017.

[29] G. Neofotistos, M. Mattheakis, G. D. Bamparis, J. Hizanidis, G. P. Tsironis, and E. Kaxiras. Machine learning with observers predicts complex spatiotemporal behavior. *arXiv preprint arXiv:1807.10758*, 2018.

[30] G. Pang, L. Lu, and G. E. Karniadakis. fPINNs: Fractional physics-informed neural networks. *SIAM Journal on Scientific Computing*, 41(4):A2603–A2626, 2019.

[31] J. C. Patra, R. N. Pal, B. Chatterji, and G. Panda. Identification of nonlinear dynamic systems using functional link artificial neural networks. *IEEE Transactions on Systems, Man, and Cybernetics, Part B (Cybernetics)*, 29(2):254–262, 1999.

[32] I. Podlubny. *Fractional differential equations: an introduction to fractional derivatives, fractional differential equations, to methods of their solution and some of their applications*. Elsevier, 1998.

[33] T. Qin, K. Wu, and D. Xiu. Data driven governing equations approximation using deep neural networks. *Journal of Computational Physics*, 2019.

[34] M. Raissi, P. Perdikaris, and G. E. Karniadakis. Multistep neural networks for data-driven discovery of nonlinear dynamical systems. *arXiv preprint arXiv:1801.01236*, 2018.

[35] F. Rossi and B. Conan-Guez. Functional multi-layer perceptron: A non-linear tool for functional data analysis. *Neural Networks*, 18(1):45–60, 2005.

[36] S. H. Rudy, S. L. Brunton, J. L. Proctor, and J. N. Kutz. Data-driven discovery of partial differential equations. *Science Advances*, 3(4):e1602614, 2017.

[37] Zhi-zhong Sun and Xiaonan Wu. A fully discrete difference scheme for a diffusion-wave system. *Applied Numerical Mathematics*, 56(2):193–209, 2006.

[38] K. S. Tai, P. Bailis, and G. Valiant. Equivariant transformer networks. *arXiv preprint arXiv:1901.11399*, 2019.

- [39] E. Teller. *The pursuit of simplicity*. Pepperdine University Press, 1981.
- [40] N. Trask, R. G. Patel, B. J. Gross, and P. J. Atzberger. GMLS-Nets: A framework for learning from unstructured data. *arXiv preprint arXiv:1909.05371*, 2019.
- [41] A. Vaswani, N. Shazeer, N. Parmar, J. Uszkoreit, L. Jones, A. N. Gomez, L. Kaiser, and I. Polosukhin. Attention is all you need. In *Advances in Neural Information Processing Systems*, pages 5998–6008, 2017.
- [42] B. J. West. *Fractional Calculus View of Complexity: Tomorrow’s Science*. CRC Press, 2016.
- [43] N. Winovich, K. Ramani, and G. Lin. ConvPDE-UQ: Convolutional neural networks with quantified uncertainty for heterogeneous elliptic partial differential equations on varied domains. *Journal of Computational Physics*, 2019.
- [44] M. Zayernouri and G. E. Karniadakis. Fractional Sturm–Liouville eigen-problems: theory and numerical approximation. *Journal of Computational Physics*, 252:495–517, 2013.
- [45] D. Zhang, L. Lu, L. Guo, and G. E. Karniadakis. Quantifying total uncertainty in physics-informed neural networks for solving forward and inverse stochastic problems. *Journal of Computational Physics*, 397:108850, 2019.
- [46] Z. Zhang and G. E. Karniadakis. *Numerical methods for stochastic partial differential equations with white noise*. Springer, 2017.
- [47] Z. Zhang, F. Zeng, and G. E. Karniadakis. Optimal error estimates of spectral Petrov-Galerkin and collocation methods for initial value problems of fractional differential equations. *SIAM Journal on Numerical Analysis*, 53(4):2074–2096, 2015.
- [48] H. Zhao and J. Zhang. Nonlinear dynamic system identification using pipelined functional link artificial recurrent neural network. *Neurocomputing*, 72(13-15):3046–3054, 2009.
- [49] Y. Zhu, N. Zabaras, P.-S. Koutsourelakis, and P. Perdikaris. Physics-constrained deep learning for high-dimensional surrogate modeling and uncertainty quantification without labeled data. *Journal of Computational Physics*, 394:56–81, 2019.

S1 Neural networks to approximate nonlinear operators

We list in Table S1 the main symbols and notations that are used throughout this paper.

Table S1: **Notation.**

X	a Banach space with norm $\ \cdot\ _X$
\mathbb{R}^d	Euclidean space of dimension d
K	a compact set in a Banach space
$C(K)$	Banach space of all continuous functions defined on K with norm $\ f\ _{C(K)} = \max_{x \in K} f(x) $
V	a compact set in $C(K)$
$u(x)$	an input function/signal
$s(x)$	an output function/signal
f	a function or functional
G	an operator
(TW)	all the Tauber-Wiener functions
σ	an activation function
$\{x_1, x_2, \dots, x_m\}$	m sensor points
n, p	neural network size hyperparameters in Theorems S4 and S5 below
N	number of basis functions
M	value of some upper bound

Let $C(K)$ denote the Banach space of all continuous functions defined on a compact set $K \subset X$ with sup-norm $\|f\|_{C(K)} = \max_{x \in K} |f(x)|$, where X is a Banach space. We first review the definition and sufficient condition of Tauber-Wiener (TW) functions [7], and the definition of continuous operator.

Definition S1 (TW). *If a function $\sigma : \mathbb{R} \rightarrow \mathbb{R}$ (continuous or discontinuous) satisfies that all the linear combinations $\sum_{i=1}^N c_i \sigma(\lambda_i x + \theta_i)$, $\lambda_i \in \mathbb{R}$, $\theta_i \in \mathbb{R}$, $c_i \in \mathbb{R}$, $i = 1, 2, \dots, N$, are dense in every $C([a, b])$, then σ is called a Tauber-Wiener (TW) function.*

Theorem S2 (Sufficient condition for TW). *Suppose that σ is a continuous function, and $\sigma \in S'(\mathbb{R})$ (tempered distributions), then $\sigma \in (TW)$, if and only if σ is not a polynomial.*

It is easy to verify that all the activation functions we used nowadays, such as sigmoid, tanh and ReLU, are TW functions.

Definition S3 (Continuity). *Let G be an operator between topological spaces X and Y . We call G continuous if for every $\epsilon > 0$, there exists a constant $\delta > 0$ such that*

$$\|G(x) - G(y)\|_Y < \epsilon$$

for all $x, y \in X$ satisfying $\|x - y\|_X < \delta$.

We recall the following two main theorems of approximating nonlinear continuous functionals and operators due to Chen & Chen [7].

Theorem S4 (Universal Approximation Theorem for Functional). *Suppose that $\sigma \in (TW)$, X is a Banach Space, $K \subset X$ is a compact set, V is a compact set in $C(K)$, f is a continuous*

functional defined on V , then for any $\epsilon > 0$, there are a positive integer n, m points $x_1, \dots, x_m \in K$, and real constants c_i, θ_i, ξ_{ij} , $i = 1, \dots, n$, $j = 1, \dots, m$, such that

$$\left| f(u) - \sum_{i=1}^n c_i \sigma \left(\sum_{j=1}^m \xi_{ij} u(x_j) + \theta_i \right) \right| < \epsilon$$

holds for all $u \in V$.

Theorem S5 (Universal Approximation Theorem for Operator). Suppose that $\sigma \in (TW)$, X is a Banach Space, $K_1 \subset X$, $K_2 \subset \mathbb{R}^d$ are two compact sets in X and \mathbb{R}^d , respectively, V is a compact set in $C(K_1)$, G is a nonlinear continuous operator, which maps V into $C(K_2)$, then for any $\epsilon > 0$, there are positive integers n, p, m , constants $c_i^k, \xi_{ij}^k, \theta_i^k, \zeta_k \in \mathbb{R}$, $w_k \in \mathbb{R}^d$, $x_j \in K_1$, $i = 1, \dots, n$, $k = 1, \dots, p$, $j = 1, \dots, m$, such that

$$\left| G(u)(y) - \sum_{k=1}^p \sum_{i=1}^n c_i^k \sigma \left(\sum_{j=1}^m \xi_{ij}^k u(x_j) + \theta_i^k \right) \sigma(w_k \cdot y + \zeta_k) \right| < \epsilon$$

holds for all $u \in V$ and $y \in K_2$.

The necessary and sufficient conditions of the compactness are given by the following Arzelà-Ascoli Theorem.

Definition S6 (Uniform Boundedness). Let V be a family of real-valued functions on the set K . We call V uniformly bounded if there exists a constant M such that

$$|f(x)| \leq M$$

for all $f \in V$ and all $x \in K$.

Definition S7 (Equicontinuity). Let V be a family of real-valued functions on the set K . We call V equicontinuous if for every $\epsilon > 0$, there exists a $\delta > 0$ such that

$$|f(x) - f(y)| < \epsilon$$

for all $f \in V$ and all $x, y \in K$ satisfying $|x - y| < \delta$.

Theorem S8 (Arzelà-Ascoli Theorem). Let X be a Banach space, and $K \subset X$ be a compact set. A subset V of $C(K)$ is pre-compact (has compact closure) if and only if V is uniformly bounded and equicontinuous.

S2 Data generation

Here, we list the details of function spaces V and reference solutions.

Gaussian random fields (GRFs). In most examples, we use the mean-zero GRFs for the input function $u(x)$:

$$u(x) \sim \mathcal{GP}(0, k_l(x_1, x_2)),$$

where the covariance kernel $k_l(x_1, x_2) = \exp(-\|x_1 - x_2\|^2/2l^2)$ is the Gaussian kernel with a length-scale parameter $l > 0$. The length-scale l determines the smoothness of the sampled function, and larger l leads to smoother u .

Orthogonal polynomials. Let $M > 0$ and P_i be i -th orthogonal polynomial basis. We define the N -dimensional orthogonal polynomial space as

$$V_{\text{Org}} = \left\{ \sum_{i=0}^{N-1} a_i P_i(x) : |a_i| \leq M \right\}.$$

We generate the samples of input function $u(\cdot)$ from the space V_{Org} by randomly sampling the expansion coefficient a_i from $[-M, M]$.

In the paper, we consider four different bases $P_i(\cdot)$:

1. the Chebyshev polynomial of the first kind $T_i(x)$;
2. the Legendre polynomial $L_i(x)$;
3. the poly-fractonomial polynomial $(1+x)^{0.5} J_i^{-0.5, 0.5}(x)$, where $J_i^{\alpha, \beta}(x)$ is the Jacobi polynomial of degree i ;
4. the Zernike polynomial $Z_i(r, \theta)$, where $Z_i(r, \theta)$ is the single indexing Zernike polynomial whose index i is linked to the indices of double-indexing one $Z_n^m(r, \theta)$ by $i = \frac{n(n+2)+m}{2}$.

Reference solutions. The reference solutions of all ODE systems are obtained by Runge-Kutta (4, 5), and the reference solutions of all deterministic PDEs are obtained by a second-order finite difference method.

The exact solution of the stochastic ODE is

$$y = y_0 e^{K(t)},$$

where $K(t) = \int_0^t k(s) ds$ is again Gaussian process with mean zero.

The exact solution of the stochastic PDE is

$$u(x) = C(\omega) \int_0^x e^{-b(y; \omega)} dy - \int_0^x \int_0^y e^{-b(z; \omega)} f(z) dz dy,$$

where

$$C(\omega) = \left(\int_0^1 e^{-b(y; \omega)} dy \right)^{-1} \int_0^1 \int_0^y e^{-b(z; \omega)} f(z) dz dy.$$

Numerical solutions are obtained by approximating $k(t; \omega)$ or $b(x; \omega)$ with their truncated Karhunen-Loeve expansions.

Remark. We note that one data point is a triplet $(u, y, G(u)(y))$, and thus one specific input u may appear in multiple data points with different values of y . For example, a dataset of size 10000 may only be generated from 100 u trajectories, and each evaluates $G(u)(y)$ for 100 y locations.

S3 Gaussian random field with the Gaussian kernel

Suppose that $X(t) \sim \mathcal{GP}(0, \exp(-\frac{|x-y|^2}{l^2}))$. Then, by the Wiener-Khinchin Theorem, we have

$$X(t) = \sqrt{2}(\pi)^{\frac{1}{4}} \int_{\mathbb{R}^+} (l)^{\frac{1}{2}} \cos(\omega t) \exp(-\frac{l^2 \omega^2}{8}) dW(\omega) - \sqrt{2}(\pi)^{\frac{1}{4}} \int_{\mathbb{R}^+} (l)^{\frac{1}{2}} \sin(\omega t) \exp(-\frac{l^2 \omega^2}{8}) dB(\omega),$$

where W and B are independent standard Brownian motions [46]. Apply the change of variable $\lambda = l\omega$ and write $X(t)$ as

$$X(t) = \sqrt{2}(\pi)^{\frac{1}{4}} \int_{\mathbb{R}^+} \cos(\frac{\lambda}{l}t) \exp(-\frac{\lambda^2}{8}) dW(\lambda) - \sqrt{2}(\pi)^{\frac{1}{4}} \int_{\mathbb{R}^+} \sin(\frac{\lambda}{l}t) \exp(-\frac{\lambda^2}{8}) dB(\lambda).$$

Applying a linear interpolation Π_1 on the interval $[t_i, t_{i+1}]$, then

$$\begin{aligned} \mathbb{E}[(X(t) - \Pi_1 X(t))^2] &= 2(\pi)^{\frac{1}{2}} \int_{\mathbb{R}^+} ((I - \Pi_1) \cos(\frac{\lambda}{l}t))^2 \exp(-\frac{\lambda^2}{4}) d\lambda \\ &\quad + 2(\pi)^{\frac{1}{2}} \int_{\mathbb{R}^+} ((I - \Pi_1) \sin(\frac{\lambda}{l}t))^2 \exp(-\frac{\lambda^2}{4}) d\lambda \\ &\leq (\pi)^{\frac{1}{2}} (t_{i+1} - t_i)^4 \int_{\mathbb{R}^+} (\frac{\lambda}{l})^4 \exp(-\frac{\lambda^2}{4}) d\lambda \\ &= 24\pi \frac{(t_{i+1} - t_i)^4}{l^4}, \end{aligned}$$

where we recalled the error estimate of the linear interpolation on $[a, b]$ (by Taylor's expansion)

$$|(I - \Pi_1)g(t)| = \frac{1}{2}(b - a)^2 |g''(\xi)|,$$

where ξ lies in between a and b . Then by the fact that $X(t) - \Pi_1 X(t)$ is Gaussian, we have

$$|X(t) - \Pi_1 X(t)| \leq C \frac{(t_{i+1} - t_i)^2}{l^2}, \quad \epsilon > 0, t \in [t_i, t_{i+1}],$$

where C is an absolute value of a Gaussian random variable with mean zero and variance $\sqrt{(24\pi)}$. In conclusion, taking a piecewise linear interpolation of $X(t)$ with m points will lead to convergence with order $\mathcal{O}(\frac{1}{m^2 l^2})$.

S4 Number of sensors for identifying nonlinear dynamical systems

This part is the proof of Theorem 2. All the concepts and notations involved here are defined in the paragraph of Theorem 2.

Lemma. $W := \bigcup_{i=1}^{\infty} W_i$ is compact.

Proof. At first, we prove that W is pre-compact. For any $\varepsilon > 0$, by (3), there exists an m_0 such that

$$\|u - \mathcal{L}_m(u)\|_C < \frac{\varepsilon}{4}, \quad \forall u \in V, \forall m > m_0.$$

Since W_{m_0} is a compact set subject to equicontinuity, there exists a $\delta > 0$ such that

$$|x - y| < \delta \Rightarrow |u(x) - u(y)| < \frac{\varepsilon}{2}, \quad \forall u \in W_{m_0}, \forall x, y \in [a, b].$$

Now for all $u \in W$ and all $x, y \in [a, b]$, $|x - y| < \delta$, if $u \in W_{m_0}$, naturally we have $|u(x) - u(y)| < \frac{\varepsilon}{2} < \varepsilon$, otherwise, $u \in \bigcup_{i=m_0+1}^{\infty} U_i$. Suppose that $u = \mathcal{L}_m(v)$, $m > m_0$, $v \in V$, then there holds

$$\begin{aligned} |u(x) - u(y)| &= |u(x) - v(x) + v(x) - v(y) + v(y) - u(y)| \\ &\leq |\mathcal{L}_m(v)(x) - v(x)| + |v(x) - v(y)| + |\mathcal{L}_m(v)(y) - v(y)| \\ &\leq 2\|\mathcal{L}_m(v) - v\|_C + |v(x) - v(y)| \\ &< 2 \cdot \frac{\varepsilon}{4} + \frac{\varepsilon}{2} = \varepsilon, \end{aligned}$$

which shows the quicontinuity of W . In addition, it is obvious that W is uniformly bounded, so that we know W is pre-compact by applying the Arzelà-Ascoli Theorem.

Next we show that W is closed. Let $\{w_i\}_{i=1}^{\infty} \subset W$ be a sequence which converges to a $w_0 \in C[a, b]$. If there exists an m such that $\{w_i\} \subset W_m$, then $w_0 \in W_m \subset W$. Otherwise, there is a subsequence $\{\mathcal{L}_{i_n}(v_{i_n})\}$ of $\{w_i\}$ such that $v_{i_n} \in V$ and $i_n \rightarrow \infty$ as $n \rightarrow \infty$. Then we have

$$\begin{aligned} \|v_{i_n} - w_0\|_C &= \|v_{i_n} - \mathcal{L}_{i_n}(v_{i_n}) + \mathcal{L}_{i_n}(v_{i_n}) - w_0\|_C \\ &\leq \|v_{i_n} - \mathcal{L}_{i_n}(v_{i_n})\|_C + \|\mathcal{L}_{i_n}(v_{i_n}) - w_0\|_C \\ &\leq \kappa(i_n, V) + \|\mathcal{L}_{i_n}(v_{i_n}) - w_0\|_C, \end{aligned}$$

which implies that $w_0 = \lim_{n \rightarrow \infty} v_{i_n} \in V \subset W$. □

Next we show the proof of Theorem 2.

Proof. For $u \in V$ and $u_m \in U_m$, according to the bound (3) and the Lipschitz conditions of the right-hand side of the ODE, we can derive that the operator is Lipschitz continuous.

$$\begin{aligned} \|G(u)(d) - G(u_m)(d)\|_2 &\leq c \int_a^d \|G(u)(t) - G(u_m)(t)\|_2 dt + c \int_a^d |u(t) - u_m(t)| dt \\ &\leq c \int_a^d \|G(u)(t) - G(u_m)(t)\|_2 dt + c(b-a)\kappa(m, V). \end{aligned}$$

Here $\kappa(m, V)$ is defined in (3). By Grönwall's inequality, we have

$$\|G(u)(d) - G(u_m)(d)\|_2 \leq c(b-a)\kappa(m, V)e^{c(b-a)}.$$

Define $S_m = \{(u(x_0), u(x_1), \dots, u(x_m)) \in \mathbb{R}^{m+1} | u \in V\}$. Then S_m is a compact set in \mathbb{R}^{m+1} as it is the image of a continuous map on the compact set V . As there is a bijective map between S_m and U_m , we may define a vector-valued function φ on S_m by

$$\varphi(u(x_0), u(x_1), \dots, u(x_m)) = G(u_m)(d).$$

Because G is a continuous operator over V , φ is a continuous function over S_m . For any $\varepsilon > 0$, make m large enough so that $c(b-a)\kappa(m, V)e^{c(b-a)} < \varepsilon$. By the universal approximation theorem of neural network for high-dimensional functions, there exist $\mathcal{W}_1 \in \mathbb{R}^{n \times (m+1)}$, $b_1 \in \mathbb{R}^{m+1}$, $\mathcal{W}_2 \in \mathbb{R}^{K \times n}$, $b_2 \in \mathbb{R}^K$, such that

$$\|\varphi(u(x_0), \dots, u(x_m)) - (\mathcal{W}_2 \cdot \sigma(\mathcal{W}_1 \cdot [u(x_0) \dots u(x_m)]^T + b_1) + b_2)\|_2 < \varepsilon - c(b-a)\kappa(m, V)e^{c(b-a)}$$

holds for all $(u(x_0), \dots, u(x_m)) \in S_m$. Hence, we have

$$\begin{aligned} & \| (Gu)(d) - (\mathcal{W}_2 \cdot \sigma(\mathcal{W}_1 \cdot [u(x_0) \dots u(x_m)]^T + b_1) + b_2) \|_2 \\ & \leq \| (Gu)(d) - (Gu_m)(d) \|_2 + \| (Gu_m)(d) - (\mathcal{W}_2 \cdot \sigma(\mathcal{W}_1 \cdot [u(x_0) \dots u(x_m)]^T + b_1) + b_2) \|_2 \\ & < c(b-a)\kappa(m, V)e^{c(b-a)} + \varepsilon - c(b-a)\kappa(m, V)e^{c(b-a)} = \varepsilon. \end{aligned}$$

In summary, by choosing the value of m so that it makes $c(b-a)\kappa(m, V)e^{c(b-a)}$ less than ε is sufficient to achieve accuracy ε . \square

S5 Parameters

In all problems we use ReLU activation function, except that for fractional differential operators we use the hyperbolic tangent. We use the Adam optimizer [20] with learning rate 0.001, except that for the Legendre transform it is 0.0001. The other parameters and network sizes are listed in Tables S2 and S3, unless otherwise stated.

Table S2: **Default parameters for each problem, unless otherwise stated.** We note that one data point is a triplet $(u, y, G(u)(y))$, and thus one specific input u may generate multiple data points with different values of y .

Case	Input function space	# Sensors m	# Training	# Test	# Iterations
Antiderivative	GRF ($l = 0.2$)	100	10^4	10^5	5×10^4
Legendre transform	GRF ($l = 0.2$)	200	10^4	2×10^4	2×10^6
Fractional (1D)	–	15	10^6	10^6	3×10^4
Fractional (2D)	Zernike	225	1.125×10^7	1.125×10^7	5×10^3
Nonlinear ODE	GRF ($l = 0.2$)	100	10^4	10^5	10^5
Gravity pendulum	GRF ($l = 0.2$)	100	10^4	10^5	10^5
Diffusion-reaction	GRF ($l = 0.2$)	100	–	10^6	5×10^5
Advection	GRF	100	5×10^4	10^5	5×10^5
Advection-diffusion	GRF ($l = 0.5$)	100	5×10^4	10^5	5×10^5
Stochastic ODE/PDE	–	20	10^6	10^6	5×10^4

Table S3: **DeepONet size for each problem, unless otherwise stated.**

Case	Trunk depth	Trunk width	Branch depth	Branch width
Antiderivative	3	40	2	40
Legendre transform	3	100	2	100
Fractional (1D)	3	40	2	40
Fractional (2D)	3	60	2	60
Nonlinear ODE	3	40	2	40
Gravity pendulum	3	40	2	40
Diffusion-reaction	3	100	2	100
Advection	3	100	2	100
Advection-diffusion	3	100	2	100
Stochastic ODE/PDE	3	100	2	100

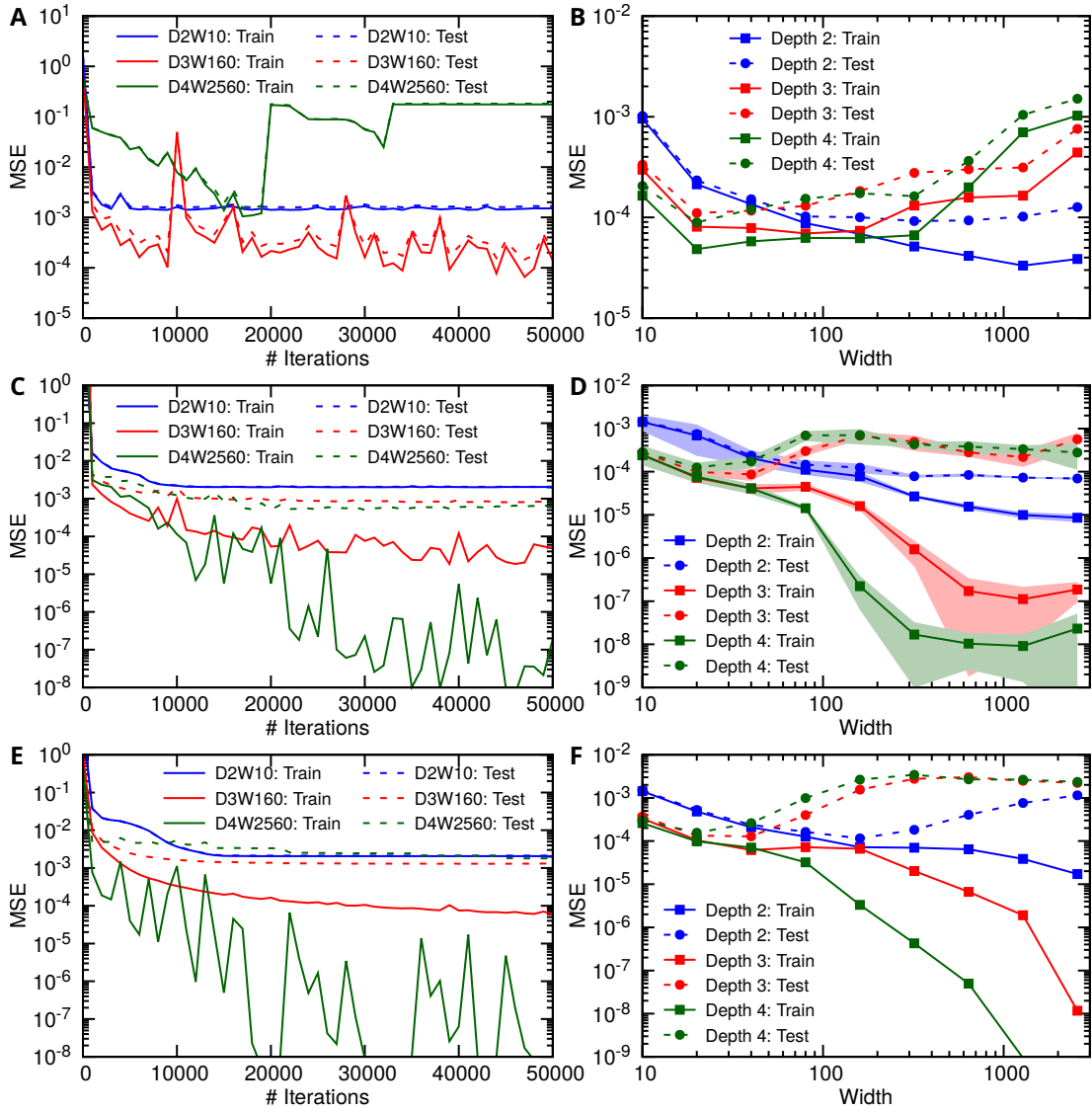


Fig. S1: **Errors of FNNs trained to learn the antiderivative operator (linear case).** (A and B) Learning rate 0.01. (C and D) Learning rate 0.001. (E and F) Learning rate 0.0001. (A, C, E) The solid and dash lines are the training error and test error during the training process, respectively. The blue, red and green lines represent FNNs of size (depth 2, width 10), (depth 3, width 160), and (depth 4, width 2560), respectively. (B, D, F) The blue, red and green lines represent FNNs of depth 2, 3 and 4, respectively. The shaded regions in (D) are the one-standard-deviation (SD) from 10 runs with different training/test data and network initialization. For clarity, only the SD of learning rate 0.001 is shown (Fig. D). The number of sensors for u is $m = 100$.

S6 Legendre transform

We consider the Legendre transform of a function $f(x)$:

Problem 7 $\mathcal{J}_n\{f(x)\} = \int_{-1}^1 P_n(x) f(x) dx,$ (S6)

where $P_n(x)$ is a Legendre polynomial of degree n . We use DeepONet to learn the Legendre transform $f(x) \mapsto \mathcal{J}_n\{f(x)\}$. Because the Legendre transform decays fast to zero w.r.t. n for a smooth $f(x)$, it is sufficient to consider the first 20 coefficients, i.e., $n \in \{0, 1, 2, \dots, 19\}$. To generate the dataset, we sampled 500 random $f(x)$ from a GRF with the Gaussian kernel of the length scale $l = 0.2$, and computed the Legendre transform at the first 20 coefficients for each $f(x)$. Thus the dataset size is equal to 10000 ($= 500 \times 20$). The test MSE is $3.2 \times 10^{-7} \pm 1.9 \times 10^{-7}$, and two prediction examples are shown in Fig. S2.

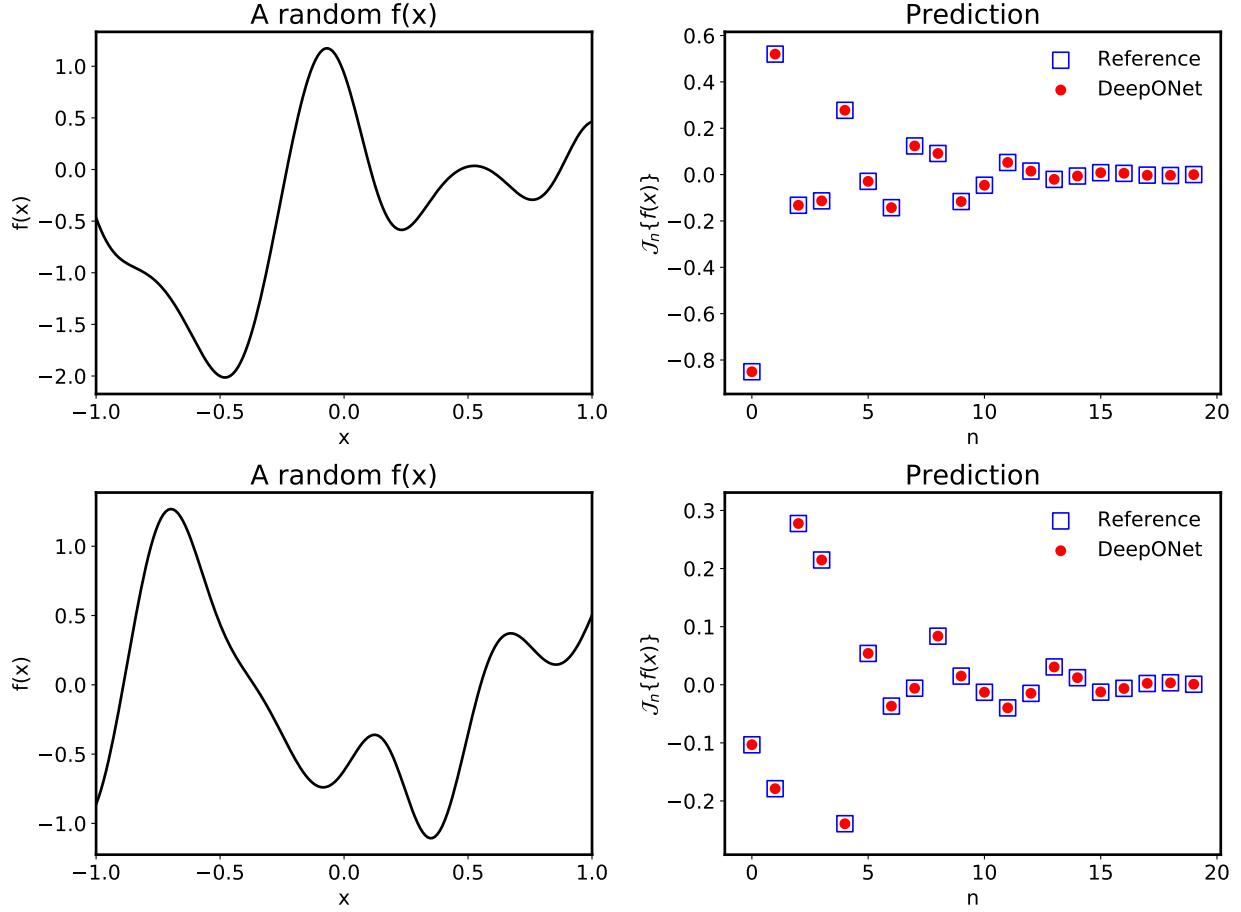


Fig. S2: DeepONet prediction of the Legendre transform for two random $f(x)$.

S7 Nonlinear ODE system

We consider a nonlinear 1D ODE system

Problem 1.C $\frac{ds(x)}{dx} = g(s(x), u(x), x)$, $x \in (0, 1]$, where $g(s(x), u(x), x) = -s^2(x) + u(x)$,

with an initial condition $s(0) = 0$. Because $s(x)$ may explode for certain u , we compute the test MSE by removing the 1% worst predictions. During the network training, the training MSE and test MSE of both stacked and unstacked DeepONets decrease, but the correlation between training MSE and test MSE of unstacked DeepONets is tighter (Fig. S3A), i.e., smaller generalization error. This tight correlation between training and test MSE of unstacked DeepONets is also observed across multiple runs with random training dataset and network initialization (Fig. S3B). Moreover, the test MSE and training MSE of unstacked DeepONets follow almost a linear correlation

$$\text{MSE}_{\text{test}} \approx 10 \times \text{MSE}_{\text{train}} - 10^{-4}.$$

Fig. S3C shows that unstacked DeepONets have smaller test MSE due to smaller generalization error. DeepONets work even for out-of-distribution predictions, see three examples of the prediction in Fig. S4.

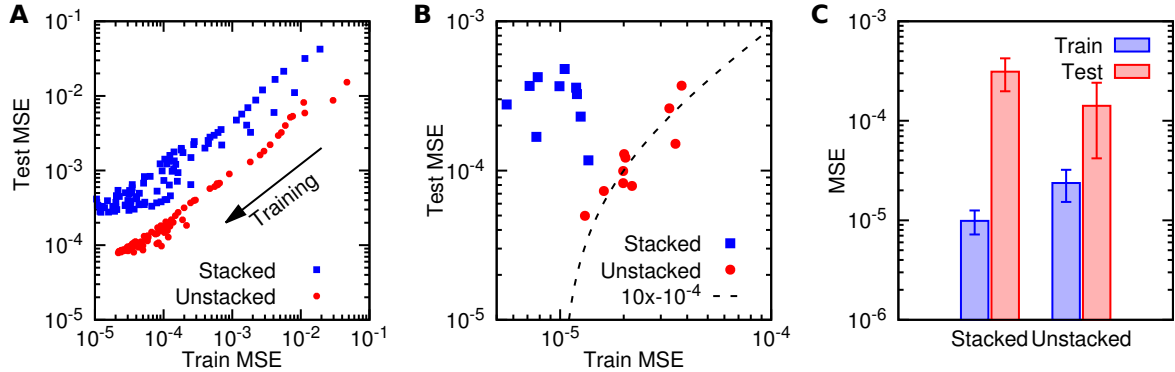


Fig. S3: Nonlinear ODE: unstacked DeepONets have smaller generalization error and smaller test MSE than stacked DeepONets. (A) The correlation between the training MSE and the test MSE of one stacked/unstacked DeepONet during the training process. (B) The correlation between the final training MSE and test MSE of stacked/unstacked DeepONets in 10 runs with random training dataset and network initialization. The training and test MSE of unstacked DeepONets follow a linear correlation (black dash line). (C) The mean and one-standard-deviation of data points in B.

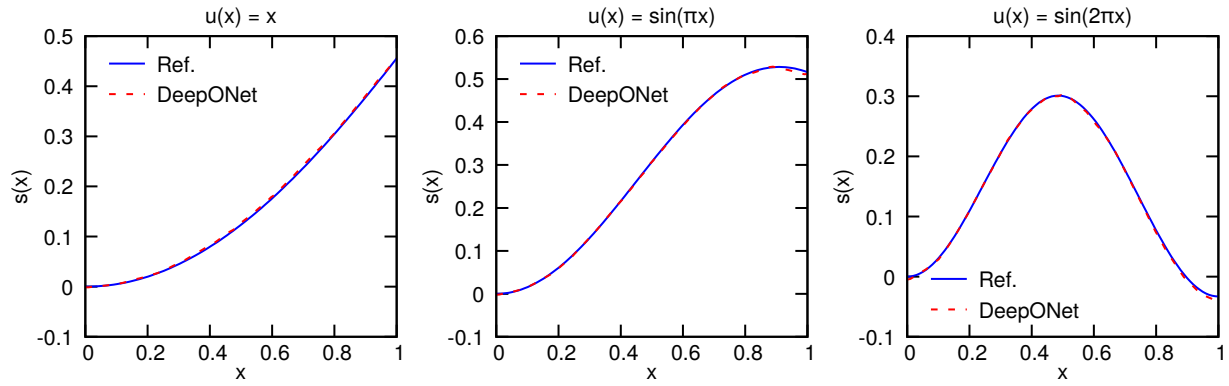


Fig. S4: **Nonlinear ODE: predictions of a trained unstacked DeepONet on three out-of-distribution input signals.** The blue and red lines represent the reference solution and the prediction of a DeepONet.

S8 Gravity pendulum with an external force

S8.1 Number of sensors

The number of sensors required to distinguish two input functions depends on the value of k , prediction time T , and the input function space. For the case with the default parameters $k = 1$, $T = 1$ and $l = 0.2$, when the number of sensors m is small, the error decays exponentially as we increase the number of sensors (Fig. S5A):

$$\text{MSE} \propto 4.6^{-\#\text{sensors}}.$$

When m is already large, the effect of increasing m is negligible. The transition occurs at ~ 10 sensors, as indicated by the arrow.

To predict s for a longer time, more sensors are required (Fig. S5B). For example, predicting until $T = 5$ requires ~ 25 sensors. If the function u is less smooth corresponding to smaller l , it also requires more sensors (Fig. S5C). However, the number of sensors is not sensitive to k (Fig. S5D). Although it is hard to quantify the exact dependency of m on T and l , by fitting the computational results we show that

$$m \propto \sqrt{T} \quad \text{and} \quad m \propto l^{-1}.$$

In Theorem 2, m should be large enough to make $Te^{cT}\kappa(m, V)$ small. In Section S3 we show theoretically that $m \propto l^{-1}$ for the GRF function space with the RBF kernel, which is consistent with our computational result here. Te^{cT} in the bound is loose compared to the computational results.

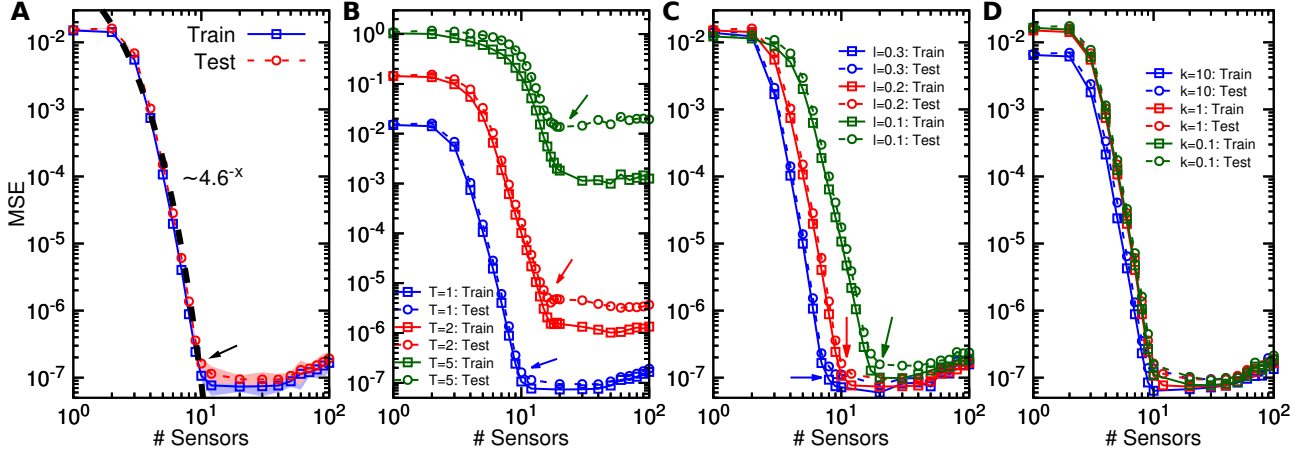


Fig. S5: **Gravity pendulum: required number of sensors for different T , k and l .** (A) Training MSE (square symbols) and test MSE (circle symbols) decrease as the number of sensors increases in the case $k = 1$, $T = 1$ and $l = 0.2$. Training and test MSE versus the number of sensors in different conditions of (B) T , (C) l , and (D) k . For clarity, the standard deviation is not shown. The arrow indicates where the rate of the error decay diminishes.

S8.2 Error tendency and convergence

Here, we investigate the error tendency under different conditions, including network size, and training dataset size. We take $T = 3$ for the following experiments in this subsection. By varying the network width, we can observe that there is a best width to achieve the smallest error (Fig.

S6A). It is reasonable that increasing the width from 1 to 100 would decrease the error, but the error would instead increase when the width further increases. This could be due to the increased optimization error, and a better learning rate may be used to find a better network. To examine the effect of training dataset size, we choose networks of width 100 to eliminate the network size effect, and the training and test errors using different dataset size are shown in Fig. S6B. The test and generalization errors of networks with width 50 and 200 are shown in Fig. 3.

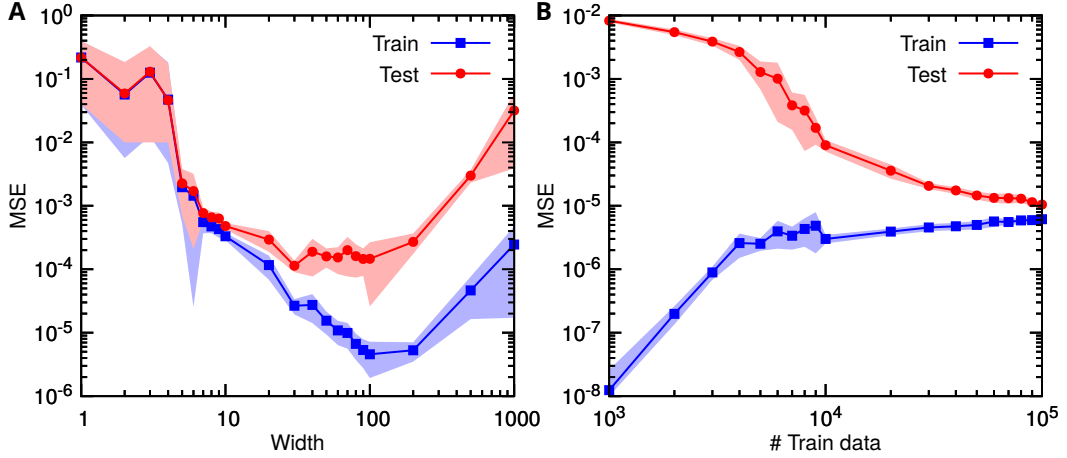


Fig. S6: **Gravity pendulum: error tendency and convergence.** (A) Training and test errors first decrease and then increase, when network width increases. (B) Test error decreases when more training data are used (width 100).

S8.3 Input function spaces

Next, we investigate the effect of different function spaces, including GRF with different length scale l and the space of Chebyshev polynomials with different number of bases. For a fixed sensor number, we observe that there exists a critical length scale, around where the training and test errors change rapidly, see the arrows in Fig. S7A. This sharp transition around the critical value is also observed in the space of Chebyshev polynomials with different number of bases (Fig. S7B). The relations between the critical values and the sensor numbers are

$$l \propto m^{-1} \quad \text{and} \quad \#\text{Bases} \propto \sqrt{m}.$$

The inverse relation between l and m is consistent with the theoretical results in Section S3 and the computational results in Section S8.1. Therefore, when the function space complexity increases, one may increase m to capture the functions well.

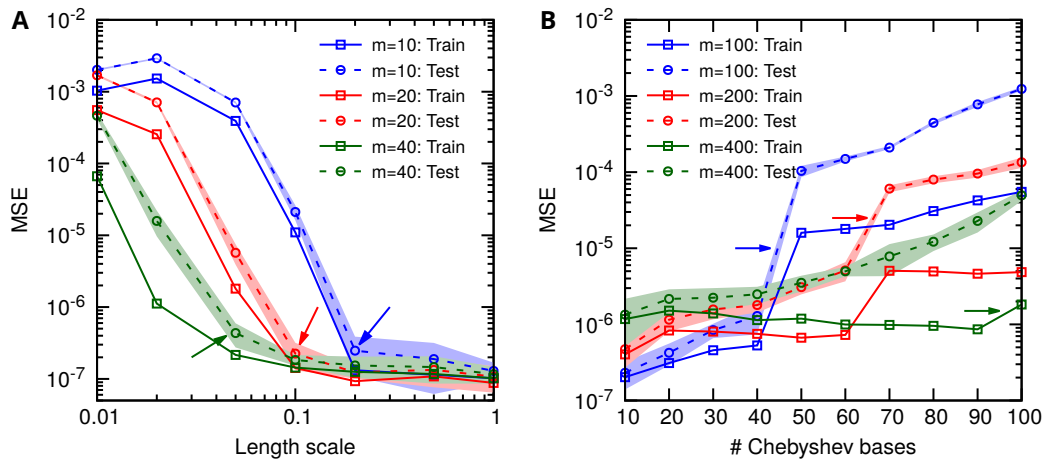


Fig. S7: **Gravity pendulum: errors for different input function spaces.** Training error (solid line) and test error (dash line) for (A) GRF function space with different length scale l . The colors correspond to the number of sensors as shown in the inset. (B) Chebyshev polynomials for different number of basis functions.

S9 Diffusion-reaction system with a source term

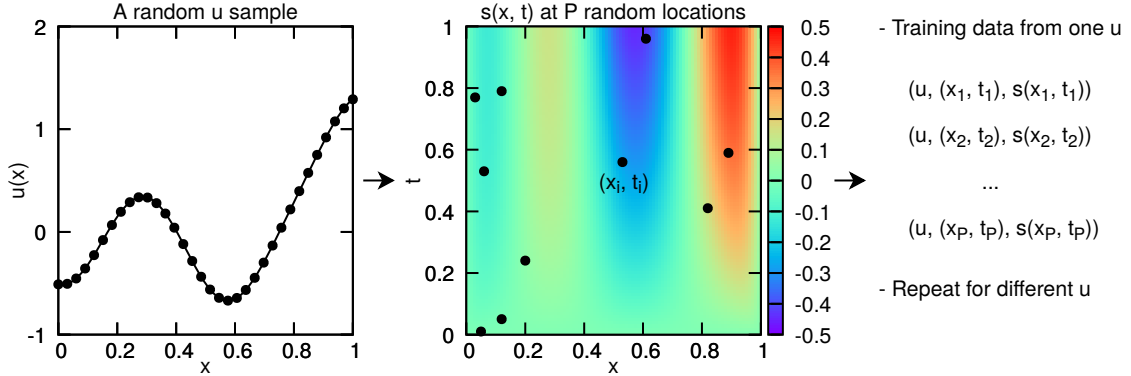


Fig. S8: **Learning a diffusion-reaction system.** (left) An example of a random sample of the input function $u(x)$. (middle) The corresponding output function $s(x, t)$ at P different (x, t) locations. (right) Pairing of inputs and outputs at the training data points. The total number of training data points is the product of P times the number of samples of u .

Table S4: **Learning a diffusion-reaction system.** Mean and standard deviation of training error and test error of ResNets from 10 independent runs.

# Residual block	Width	Training error	Test error
1	20	$2.4 \times 10^{-3} \pm 4.8 \times 10^{-4}$	$9.9 \times 10^{-2} \pm 4.8 \times 10^{-2}$
1	50	$2.4 \times 10^{-4} \pm 2.6 \times 10^{-5}$	$4.3 \times 10^{-1} \pm 1.3 \times 10^{-1}$
1	100	$2.2 \times 10^{-5} \pm 2.0 \times 10^{-6}$	$1.4 \times 10^{-1} \pm 1.8 \times 10^{-2}$
2	20	$2.2 \times 10^{-3} \pm 2.3 \times 10^{-5}$	$6.0 \times 10^{-1} \pm 1.8 \times 10^{-1}$
2	50	$5.8 \times 10^{-5} \pm 7.3 \times 10^{-6}$	$2.6 \times 10^{-1} \pm 5.6 \times 10^{-2}$
3	20	$1.1 \times 10^{-3} \pm 1.3 \times 10^{-4}$	$6.1 \times 10^{-1} \pm 3.0 \times 10^{-1}$
3	50	$2.8 \times 10^{-5} \pm 3.6 \times 10^{-6}$	$2.1 \times 10^{-1} \pm 6.4 \times 10^{-2}$

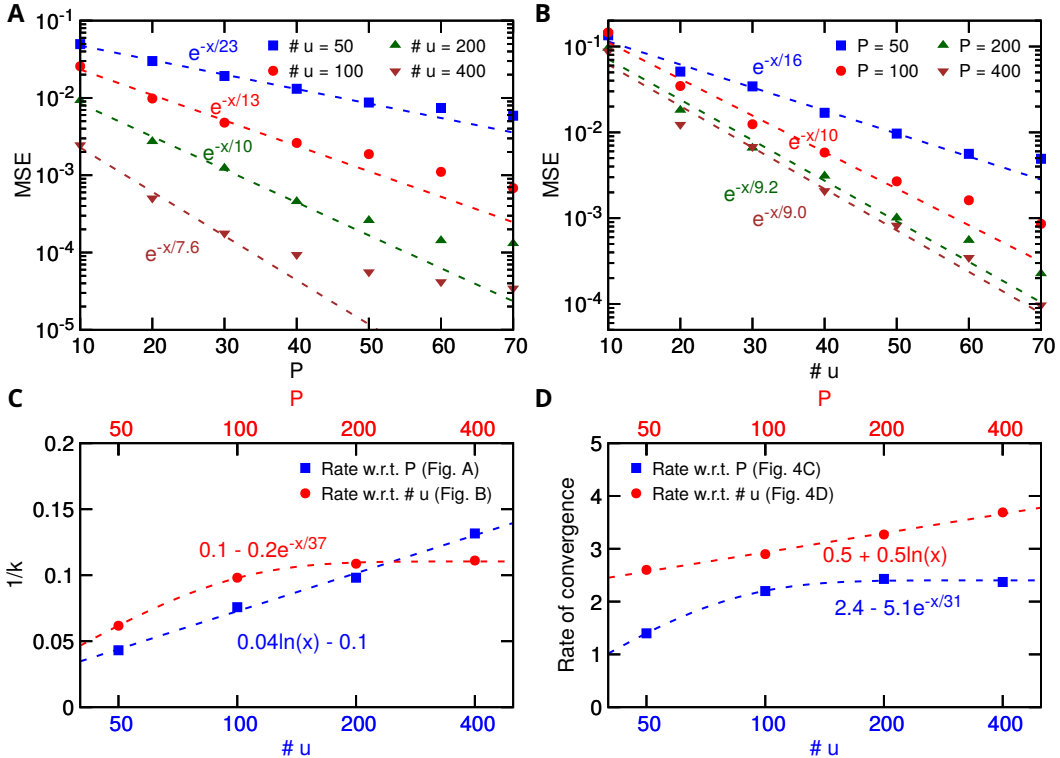


Fig. S9: **Diffusion-reaction system: error convergence rates for different number of training data points.** (A) Exponential convergence of test error with respect to P for different number of u samples. (B) Exponential convergence of test error with respect to the number of u samples for different values of P . (C) The coefficient $1/k$ in the exponential convergence $e^{-x/k}$ versus the number of u samples or the values of P . (D) The polynomial rates of convergence versus the number of u samples or the values of P .

S10 Advection equation

Consider the advection equation

$$\textbf{Problem 8} \quad \frac{\partial s}{\partial t} + a(x) \frac{\partial s}{\partial x} = 0, \quad x \in [0, 1], t \in [0, 1],$$

and here we learn four operators mapping from different input functions to the solution $s(x, t)$. The choices of $a(x)$, IC/BC and DeepONet input function are listed in Table S5. We note that in these four cases, $a(x)$ is positive. In Cases I and IV we use a periodic BC, and thus the IC is also chosen to be periodic.

To generate the training dataset, we solve the system using a finite difference method on a 100 by 100 grid, except for the Case I with the analytical solution $s(x, t) = f(\sin^2(\pi(x - t)))$. Then for each solution $s(x, t)$ we randomly select $P = 100$ points out of these 10000($= 100 \times 100$) grid points. The dataset size is equal to the product of P by the number of input function samples. We sample $f(x)$ in Table S5 from a GRF with the Gaussian kernel of different length scale l , and we use 500 random f samples for training.

Table S5: **Setup and results of four different cases of the advection equation.** Mean and standard deviation of the test MSE error are obtained from 10 independent runs.

Case	$a(x)$	IC $s(x, 0)$	BC	Input	Length scale l	Test MSE	Example
I	1	$f(\sin^2(\pi x))$	Periodic	$s(x, 0)$	0.5	$1.8 \times 10^{-6} \pm 4.2 \times 10^{-7}$	Fig. S10
II	1	$xf(x)$	$s(0, t) = 0$	$s(x, 0)$	0.2	$3.7 \times 10^{-7} \pm 1.8 \times 10^{-7}$	Fig. S11
III	$1 + 0.1 \cdot f(x)$	x^2	$s(0, t) = \sin(\pi t)$	$f(x)$	0.2	$1.6 \times 10^{-5} \pm 6.8 \times 10^{-6}$	Fig. S12
IV	$1 + 0.1 \cdot \frac{f(x) + f(1-x)}{2}$	$\sin(2\pi x)$	Periodic	$f(x)$	0.2	$3.2 \times 10^{-5} \pm 1.4 \times 10^{-5}$	Fig. S13

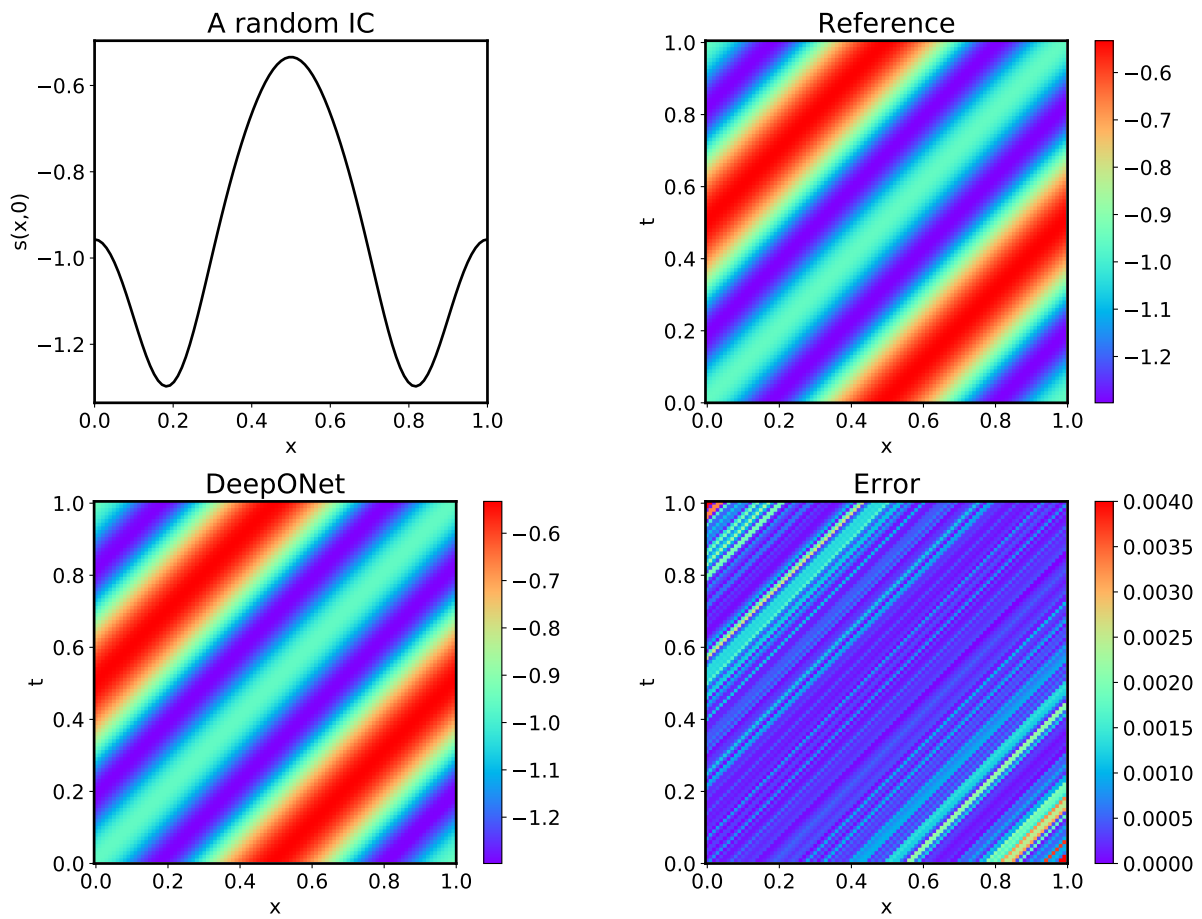


Fig. S10: DeepONet prediction of the advection equation in Case I for a random IC.

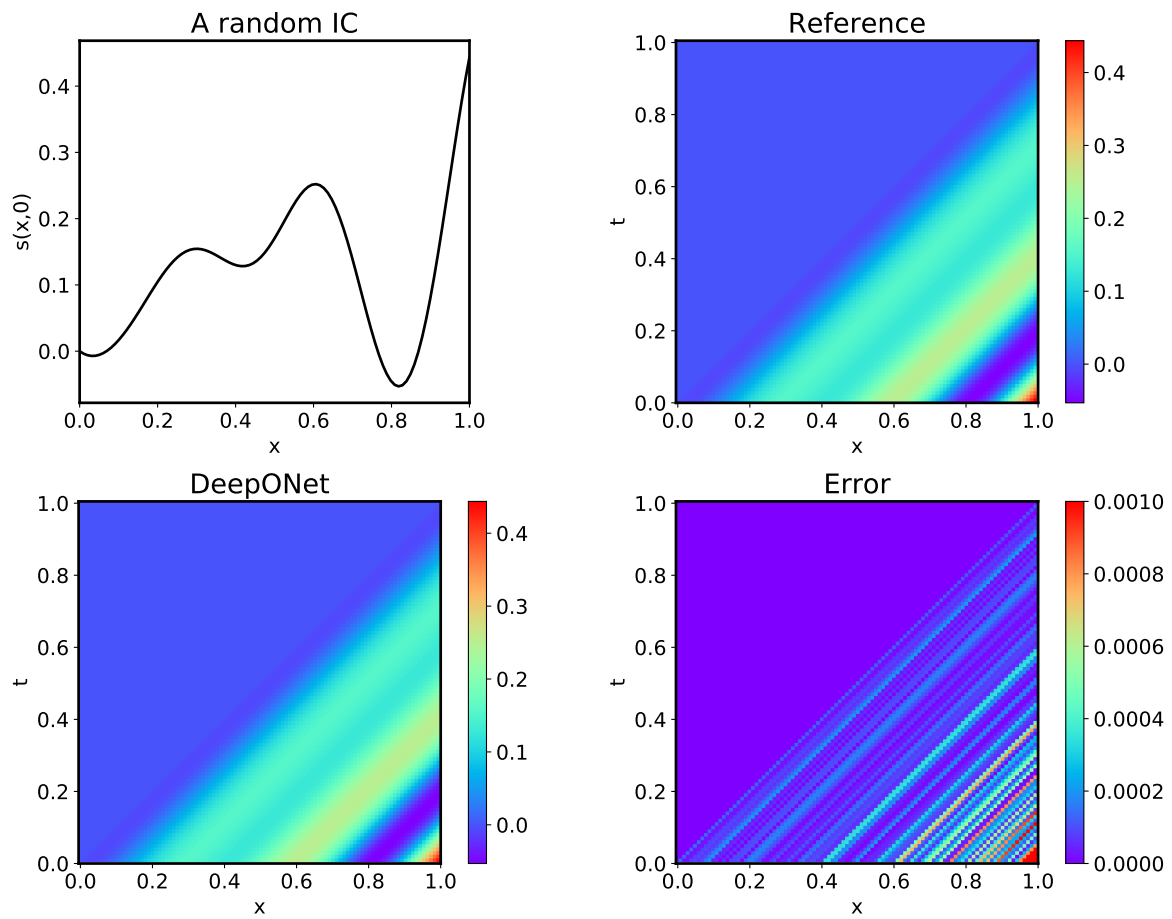


Fig. S11: **DeepONet prediction of the advection equation in Case II for a random IC.**

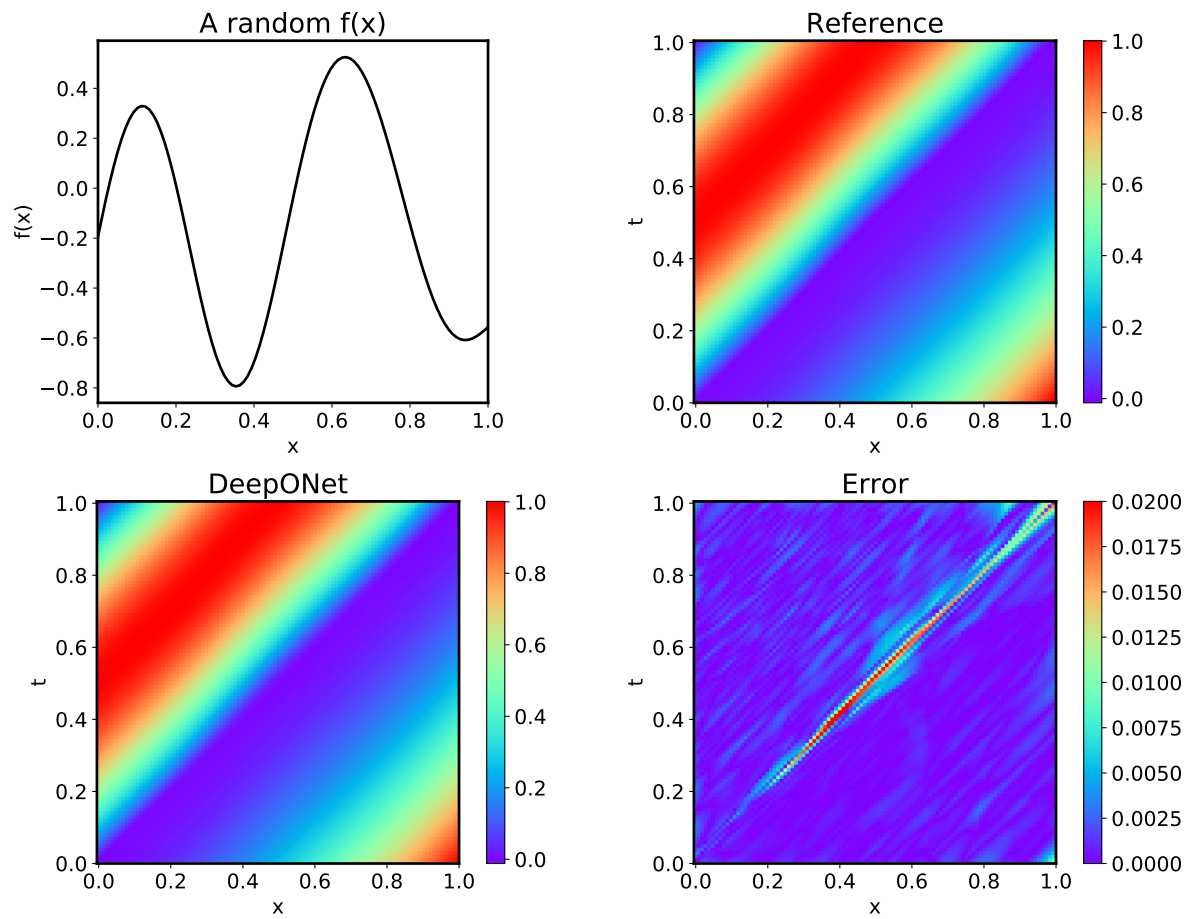


Fig. S12: **DeepONet prediction of the advection equation in Case III for a random $f(x)$.**

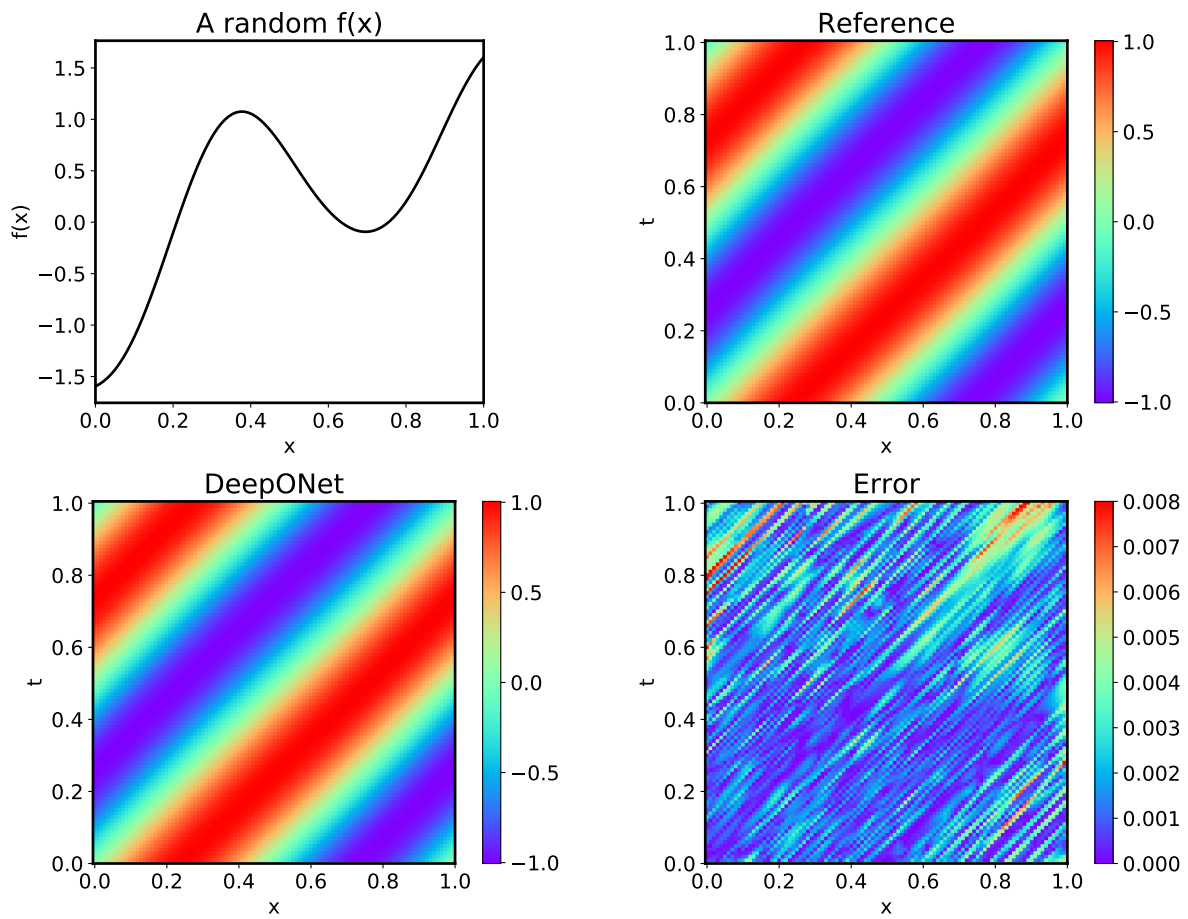


Fig. S13: **DeepONet prediction of the advection equation in Case IV for a random $f(x)$.**

S11 Advection-diffusion equation

Consider the advection-diffusion equation

Problem 9 $\frac{\partial s}{\partial t} + \frac{\partial s}{\partial x} - D \frac{\partial^2 s}{\partial x^2} = 0, \quad x \in (0, 1), t \in (0, 1],$ (S7)

with the periodic boundary condition and initial condition $s(x, 0) = f(\sin^2(\pi x))$, where $D = 0.1$ is the diffusion coefficient and $f(x)$ is sampled from a GRF with the Gaussian kernel of the length scale $l = 0.5$. Here, $s(x, 0)$ is the input function, and we use DeepONets to learn the operator mapping from $s(x, 0)$ to the solution $s(x, t)$. To generate the training dataset, we solve the system using a finite difference method on a 100 by 100 grid, and then for each solution $s(x, t)$ we randomly select $P = 100$ points out of these 10000($= 100 \times 100$) grid points. The dataset size is equal to the product of P by the number of $s(x, 0)$ samples which is set to 500 here. The test MSE is $8.7 \times 10^{-6} \pm 1.1 \times 10^{-6}$ and Fig. S14 is an example for prediction.

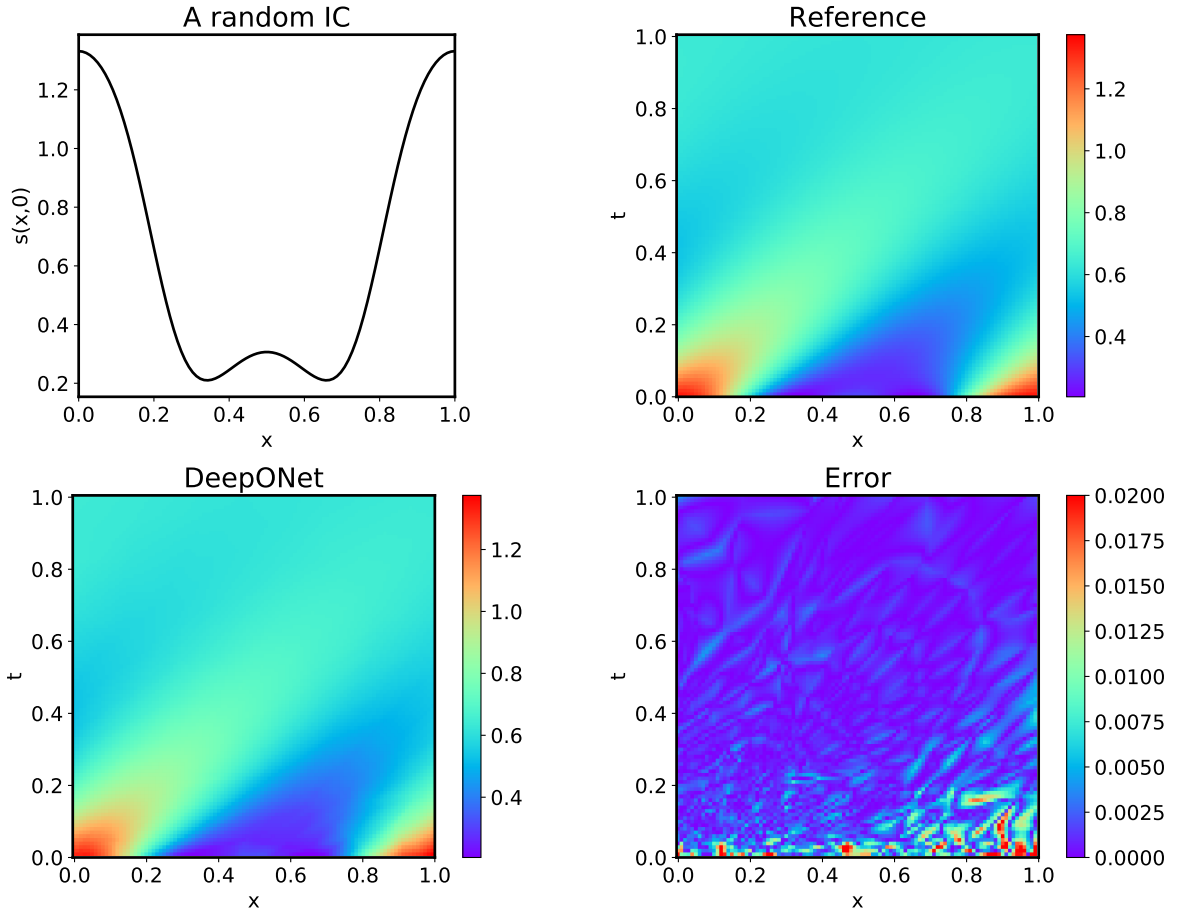


Fig. S14: DeepONet prediction of the advection-diffusion equation for a random IC.

S12 Fractional differential operators

Below we detail the data generation and NN architectures for learning the 1D Caputo fractional derivative and the 2D fractional Laplacian.

S12.1 1D Caputo derivative operator

The V spaces we consider are Legendre polynomial space, poly-fractonomial space, and GRF, all of which have been mentioned in Section S2. For the Legendre and poly-fractonomial spaces, we take $M = 2$ and $N = 11$. The expansion coefficients are taken from Sobol sequence, a quasi-random sequence. For the GRF, we set $l = 0.1$ and $l = 0.3$ in the Gaussian kernel for training and test sets, respectively.

Given the discrete version of the input function $u(\cdot)$, i.e., $[u(x_1), \dots, u(x_m)]^T$, the evaluation point y , and the fractional order α , the reference solution $G(u)(y, \alpha)$ is computed by using the $L1$ scheme [37], a finite difference scheme for approximating Caputo fractional derivative. We take 2000 finite difference points in order to ensure that the computed value of output function is sufficiently accurate.

The training set is determined by the following parameters. The number of different samples of $u(\cdot)$ is $N_u = 10000$. The number of the equi-spaced “sensors” for $u(\cdot)$ is $m = 15$. The numbers of different equi-spaced evaluation points y and α for the output function $G(u)(y, \alpha)$ are both $N_y = N_\alpha = 10$. The number of training points is calculated as $N_u \times N_y \times N_\alpha = 10^6$. The same parameters are taken for the test set.

S12.2 2D fractional Laplacian operator

The V space, where $u(r, \theta)$ is sampled from, is an orthogonal polynomial space spanned by the Zernike polynomial $Z_i(r, \theta)$, where r and θ are the radius and angle in the polar coordinate, respectively. We take 15 basis functions $\{Z_0, Z_1, \dots, Z_{14}\}$, namely, $N = 15$, and set $M = 2$ for sampling the expansion coefficients a_i in Section S2.

Given the discrete version of the input function $u(\cdot)$, i.e., $[u(x_1), \dots, u(x_m)]^T$, the evaluation point y , and the fractional order α , the reference solution $G(u)(y, \alpha)$ is computed by using the vector Grünwald-Letnikov formula [26] for approximating Riesz fractional Laplacian. We take 16 Gauss quadrature points for evaluating the integral with respect to differentiation direction and take 2000 finite difference points to approximate fractional directional derivative along a specific differentiation direction.

For DeepONet and CNN models, the raw data are the same. We choose $N_u = 5000$, $N_x = 15 \times 15 = 225$, $N_y = 15 \times 15 = 225$, and $N_\alpha = 10$. But the raw data are organized in different ways for the two models. The DeepONet model organizes the data in a loose way, and thus the size of training set is large, namely, $N_u \times N_y \times N_\alpha = 1.125 \times 10^7$. In contrast, the CNN model leverages the spatial structure of the raw data and rearranges the data into a compact form (image). The size of training set is only $N_u = 5000$. Also, the parameters for the test set are the same as those for the training one.

For the CNN, the filter size is fixed to be 3×3 , and the maxpooling window size is 2×2 . The input images are shaped to be a 4D array having the shape $[N_u, H_x, W_x, 1]$, where the height (H_x) and width (W_x) of the image for contour plot of one sample of $u(\cdot)$ are taken to be $H_x = W_x = \sqrt{N_x}$. The output images are arranged to another 4D array having the shape $[N_u, H_y, W_y, N_\alpha]$, where the height (H_y) and width (W_y) of the images for contour plots of $\{G(u)(y, \alpha_1), G(u)(y, \alpha_2), \dots, G(u)(y, \alpha_{N_\alpha})\}$ are taken to be $H_y = W_y = \sqrt{N_y}$. We denote by N_{chan} the number of channels in a convolution

layer. From the input images to the latent vector, we successively have a convolutional layer with $N_{chan} = 32$, a maxpooling layer, a convolutional layer with $N_{chan} = 64$, and a dense layer with width 64. We take zero padding and stride size 1 for all the above layers. From the latent vector to the output images, we successively have a dense layer with width 64, a dense layer with width 1024 (then reshaped to the shape $[N_u, 4, 4, 64]$), a convolutional layer with $N_{chan} = 32$, padding size 2, and stride 1 (then upsampled to the shape $[N_u, 13, 13, 1]$), and a convolutional layer with $N_{chan} = N_\alpha$, padding size 2 and stride size 1. The CNN architecture we just mentioned are rather similar to encoder and decoder in an autoencoder. We borrow the idea of latent space in the autoencoder, and link the two parts in the CNN using the latent space. The dimensionality of the latent space is set to be 20 in the current example.

S13 Hölder continuity of the operators in this work

For all the explicit and implicit operators in our examples, the operators G are Hölder continuous.

$$\|G(f) - G(g)\|_X \leq C \|f - g\|_Y^\alpha, \quad 0 < \alpha \leq 1.$$

Here $C > 0$ depends on f and g and the operator G . Here we X and Y are Banach spaces and they refers to the space of continuous functions on a compact set unless otherwise stated.

Let $G_{\mathbb{N}}$ be the approximated G using DeepONet. Let f_h be an approximation of f in Y , possibly by collocation or neural networks. Then

$$\|G(f) - G_{\mathbb{N}}(f_h)\|_X \leq \|G(f) - G(f_h)\|_X + \|G(f_h) - G_{\mathbb{N}}(f_h)\|_X \leq C \|f - f_h\|_Y^\alpha + \varepsilon,$$

where ε is the user-defined accuracy as in the universal approximation theorem by neural networks and thus the key is to verify the operator G is Hölder continuous.

The explicit operators and their Lipschitz continuity ($\alpha = 1$) are presented below.

1. (Simple ODE, **Problem 1.A**) $G(u)(x) = s_0 + \int_0^x u(s) ds$.

$$\max_{x \in [0, b]} |G(u)(x) - G(v)(x)| \leq b \max_{x \in [0, b]} |u - v|.$$

2. (Caputo derivative, **Problem 2**) The operator is Lipschitz continuous with respect to its argument in weighted Sobolev norms, c.f. [47, Theorem 2.4].
3. (Integral fractional Laplacian, **Problem 3**) The operator is Lipschitz continuous with respect to its argument in weighted Sobolev norms, c.f. [14, Theorem 3.3].
4. (Legendre transform, **Problem 7** in Equation (S6)). The Lipschitz continuity of the operator $G(u)(n) = \int_{-1}^1 P_n(x)u(x) dx$ can be seen as follows. For any non-negative integer,

$$\max_n |G(u)(n) - G(v)(n)| \leq \max_n \int_{-1}^1 |P_n(x)| dx \max_{x \in [-1, 1]} |u - v| \leq C \max_{x \in [-1, 1]} |u - v|$$

$$\text{where } C = \max_n \left(\int_{-1}^1 dx \right)^{1/2} \left(\int_{-1}^1 |P_n(x)|^2 dx \right)^{1/2} = \max_n (2 \frac{2}{2n+1})^{1/2} \leq 2.$$

5. The linear operator from **Problem 9** in (S7) in Lipschitz continuous with respect to the initial condition in the norm in the space of continuous functions, from the classical theory for linear parabolic equations [21, Chapter IV],

The implicit operators from dynamic systems and differential equations are more complicated. The Hölder continuity of these operators are elaborated in the following text.

The implicit operator from **Problem 1**. The Lipschitz continuity of the operator has been shown in the proof of Theorem 2. For Problem 1.C, the solution is still bounded as long as the input u is not too large. With a bounded solution s , the nonlinear term s^2 is Lipschitz continuous, and thus, the Lipschitz continuity of the operator is still valid, as in the proof of Theorem 2.

The implicit operator from **Problem 4** is Lipschitz with respect to the right-hand side u of not large values, from the classical theory for quasi-linear parabolic equations [21, Chapter V].

The implicit operator from **Problem 5**. $dy(t, \omega) = k(t, \omega)y(t, \omega) dt$, $y(0) = y_0$. Here $k(t)$ is a Gaussian process with mean zero and a smooth covariance function. The exact solution is

$y = y_0 \exp(\int_0^t k(s) ds)$. Then the solution operator is Lipschitz continuous in the pathwise sense. Let $k_1(t)$ and $k_2(t)$ be the coefficients in Problem 5 and $y_1(t)$ and $y_2(t)$ are the corresponding solutions. By the mean value theorem, $|e^x - e^y| \leq |x - y| (e^x + e^y)$ holds for all $x, y \in \mathbb{R}$ and

$$\begin{aligned} |y_1(t) - y_2(t)| &= |y_0| \left| \exp\left(\int_0^t k_1(s) ds\right) - \exp\left(\int_0^t k_2(s) ds\right) \right| \\ &\leq |y_0| \left(\exp\left(\int_0^t k_1(s) ds\right) + \exp\left(\int_0^t k_2(s) ds\right) \right) \left| \int_0^t k_1(s) - k_2(s) ds \right| \\ &\leq |y_0| \exp\left(\int_0^t k_1(s) ds\right) + \exp\left(\int_0^t k_2(s) ds\right) |k_1 - k_2|_{C([0,T])} \end{aligned}$$

Then for any $t \in [0, T]$,

$$\|G(k_1)(\cdot, \omega) - G(k_2)(\cdot, \omega)\|_{C[0,T]} \leq C(\omega, t) |k_1(\cdot, \omega) - k_2(\cdot, \omega)|_{L^\infty([0,t])},$$

where $C(\omega, T) = |y_0| (\max_{t \in [0,T]} \exp(\int_0^t k_1(s, \omega) ds) + \max_{t \in [0,T]} \exp(\int_0^t k_2(s, \omega) ds))$ has moments of any order, according to [4, Proposition 2.3].

The implicit operator from **Problem 6**. The operator can be written as $u = G(b)$ and $u_i = G(b_i)$, $i = 1, 2$ satisfy the following equations:

$$-\operatorname{div}(e^{b_i(x)} \nabla u_i) = f(x), \quad x \in D = (0, 1), \quad u_i(x) = 0, \quad x \in \partial D,$$

Then $\|u_i(\omega)\|_{H^1} \leq (\min_{x \in D} e^{-b_i})^{-1} \|f\|_{H^{-1}}$, where H^1 and H^{-1} are standard Sobolev-Hilbert spaces. The difference $u_1 - u_2$ satisfies the following

$$-\operatorname{div}(e^{b_1(x)} \nabla (u_1 - u_2)) = \operatorname{div}((e^{b_1(x)} - e^{b_2(x)}) \nabla u_2), \quad x \in D, \quad u_1 - u_2 = 0, \quad x \in \partial D.$$

Then by the stability of the elliptic equation, we have

$$\begin{aligned} \|u_1(\omega) - u_2(\omega)\|_{H^1} &\leq (\min_{x \in D} e^{b_i(x)})^{-1} \left\| (e^{b_1} - e^{b_2}) \nabla u_2 \right\|_{L^2} \\ &= (\min_{x \in D} e^{b_1(x)})^{-1} \left\| e^{b_1} - e^{b_2} \right\|_{C(D)} \|u_2\|_{H^1} \\ &\leq (\min_{x \in D} e^{b_1(x)})^{-1} (\min_{x \in D} e^{b_2(x)})^{-1} \left\| e^{b_1} - e^{b_2} \right\|_{C(D)} \|f\|_{H^{-1}} \end{aligned}$$

Then by the mean value theorem, $|e^x - e^y| \leq |x - y| (e^x + e^y)$ holds for all $x, y \in \mathbb{R}$. Thus,

$$\|u_1(\omega) - u_2(\omega)\|_{H_0^1} \leq (\min_{x \in D} e^{b_1(x)})^{-1} (\min_{x \in D} e^{b_2(x)})^{-1} (\|e^{b_1}\|_{C(D)} + \|e^{b_2}\|_{C(D)}) \|b_1 - b_2\|_{C(D)} \|f\|_{H^{-1}}.$$

According to [4, Proposition 2.3], all the random variables $\min_{x \in D} e^{b_i(x)}$ and $\|e^{b_i}\|_{C(D)}$, $i = 1, 2$ have any moments of finite order. Then, we obtain the pathwise Lipschitz continuity of the operator G

$$\|\mathcal{G}(b_1)(\omega) - \mathcal{G}(b_2)(\omega)\|_{H^1} \leq C(\omega) \|b_1 - b_2\|_{C(D)}.$$

Here $C(\omega) = (\min_{x \in D} e^{b_1(x)})^{-1} (\min_{x \in D} e^{b_2(x)})^{-1} (\|e^{b_1}\|_{C(D)} + \|e^{b_2}\|_{C(D)}) \|f\|_{H^{-1}}$.

The implicit operator in **Problem 8** is also Lipschitz continuous. The solution can be represented as $s_0(X^{-1}(t, x))$, where $X(t, x)$ satisfies the following equation

$$\dot{X}(t, x) = a(t, X(t, x)), \quad X(0, x) = x.$$

As there exists $a_0 > 0$ such that $a(t, x) > a_0 > 0$ in the setting of Problem 8, $X(t, x) > 0$ is away from zero. Denote the solution with coefficient a and initial condition u_0 by $u_0(X_a^{-1})$ and the solution with coefficient b and initial condition v_0 by $v_0(X_b^{-1})$. We then can derive the Lipschitz continuity of the operator from the following facts that

$$u_0(X_a^{-1}(t, x)) - v_0(X_b^{-1})(t, x) = (u_0(X_a^{-1}(t, x)) - u_0(X_b^{-1}(t, x))) + (u_0(X_b^{-1}(t, x)) - v_0(X_b^{-1})(t, x))$$

and that u_0, v_0 are Lipschitz and X_a and X_a^{-1} (X_b and X_b^{-1}) are Lipschitz continuous with respect to a (b).